Composite Structures 288 (2022) 115322

Contents lists available at ScienceDirect

Composite Structures

journal homepage: www.elsevier.com/locate/compstruct

A computational multiscale model for anisotropic failure of sheet molding compound composites

Johannes Görthofer [a], Matti Schneider [a], Andrew Hrymak [b], Thomas Böhlke [a,*]

[a] Karlsruhe Institute of Technology (KIT), Institute of Engineering Mechanics, Germany
[b] University of Western Ontario (UWO), Department of Chemical and Biochemical Engineering, Canada

ARTICLE INFO

Keywords:
Continuum damage mechanics
Failure
Anisotropy
Multiscale
Bayesian optimization
Sheet molding compound composite

ABSTRACT

We present a holistic multiscale approach for constructing anisotropic criteria describing the macroscopic failure of sheet molding compound composites based on full-field simulations of microscale damage evolution. We use an anisotropic damage model on the microscale that directly operates on the compliance tensor, captures matrix and bundle damage via dedicated stress-based damage criteria and allows for a comparison of simulation and experimental results. To identify the damage material-parameters used in the non-linear and time-consuming full-field simulations, we utilize Bayesian optimization with Gaussian processes. We validate the full-field predictions on the microscale and subsequently identify macroscopic failure criteria based on distributions taken from experimental findings. We propose failure surfaces in stress space and stiffness-reduction triggered failure surfaces to cover both a structural analysis and a design process perspective.

1. Introduction

1.1. State of the art

Typically, sheet molding compound (SMC) composites are composed of a thermoset resin, reinforced by long chopped carbon or glass fibers, and further additives and fillers [1–3]. The compression molding manufacturing process allows for producing components at comparatively low costs while offering a high freedom in design [4]. SMC composites provide a high strength-to-weight ratio [5,6], making them ideally suited for lightweight applications.

The manufacturing process of SMC leads to a characteristic microstructure where fibers are almost aligned in bundles [7–9]. Combining glass and carbon fiber bundles [10–12] permits applying SMC composites as load-bearing structural components. A modern unsaturated polyester polyurethane hybrid (UPPH) resin without fillers allows to manufacture SMC composites with discontinuous glass fiber bundles and local continuous carbon fiber patch reinforcements within a simultaneous co-molding process [13,14].

The increased use of SMC composites fosters the development of accurate mechanical models [14,15]. Experimental investigations of the microstructure [9,16,17], the effective elastic behavior in a quasi-static [18,19] and dynamical setting [20–22] were performed. In-situ testing using micro-computed tomography (μCT) sheds light on the underlying damage mechanisms [1,23,24] and microcrack distributions [25,26].

The influence of temperature, especially with an eye towards the glass transition of the polymer resin, was analyzed by Kehrer et al. [22] for the elastic regime. Meyer, Hohberg and co-workers studied the flow and curing behavior during the manufacturing process [8,27]. The behavior of SMC composites under fatigue loading was studied by Larbi et al. [28] and Bartkowiak et al. [29,30]. Investigations on the structural behavior of SMC composites under combined stress states were performed via dedicated cruciform specimens [31–33]. Non-destructive measurement techniques were developed for quantifying manufacturing uncertainties and hence the quality of SMC composite parts [34–36].

Further focus of recent research on SMC composites is devoted to damage and failure. Fitoussi et al. [37,38] presented approaches for predicting anisotropic damage evolution based on multilocal criteria, also at high strain rate [39]. Matrix degradation and interface decohesion, two major damage mechanisms in SMC composites, were analyzed and modeled by Meraghni and co-workers [40,41] and implemented in a micromechanical framework [42]. A similar approach for predicting the non-linear behavior of SMC composites was proposed by Baptiste [43]. Dedicated models were developed that account for the multiscale and anisotropic nature of SMC composites [44,45], taking into account reliability [46], inclusion distributions [47,48], humidity [23] or dynamical behavior [49].

* Corresponding author.
E-mail address: thomas.boehlke@kit.edu (T. Böhlke).

https://doi.org/10.1016/j.compstruct.2022.115322
Received 19 May 2021; Accepted 27 January 2022
Available online 18 February 2022

Most micromechanics models are based on mean-field methods [50–52], e. g., taking into account a numerically computed Eshelby's tensor [53], an evaluation of inclusion stresses [54], a Weibull probability density for the interface strength [55] or a mixture of glass and carbon fibers [11]. Computational homogenization techniques [56] were used for studying the effective elastic behavior of SMC composites [57,58].

Typically, continuum damage mechanics is based on a so-called damage variable which describes the current state of damage within the material [59,60]. The damage variable is governed by an evolution equation, reflecting the progressive degradation of the material. The damage variable can be scalar, vectorial or tensorial, and is typically abstract, i. e., it does not directly mimic the underlying physics. A scalar variable is proposed to model neat epoxy resin [61], unidirectionally aligned composites [62] or composite laminae [63], vectorial variables are used in the context of composite fabrics [64] or laminates [65]. To capture the damage evolution of a fully anisotropic material, at least a fourth-order tensor damage variable is needed [60,66]. Selecting the compliance as the primary damage variable [67–69] provides an observable quantity which furthermore enables a direct comparison with experimental findings.

SMC composites typically show an elasto-damageable behavior that is driven by anisotropic damage evolution [20,31] and eventually ends in abrupt failure. Damage evolution on the microscale induces an effective stress–strain relationship characterized by a hardening, rather than a softening, regime [12,18]. Hence, no localization occurs prior to a specific loading point right before total failure of the SMC composite [15,40].

1.2. Contributions and organization of this article

In this work, we introduce a methodology for identifying anisotropic failure surfaces to be used in component-scale simulations based on computational micromechanics. The presented multiscale approach allows for a scale-transition of full-field damage evolution within matrix and fiber bundles to an experimentally supported identification of application-based failure criteria for the SMC composite on the macroscale.

With the desire to apply SMC composites as load-bearing structural components in mind, we start this work by analyzing experimental investigations as well as simulation-based studies published by different research groups. We give a brief overview of the considered SMC composite and a set of representative experimental investigations on neat UPPH and SMC composite specimens in Section 2. An analysis of μCT-based in-situ experiments offers further insight into the behavior of SMC composites during loading.

To represent the anisotropic elasto-damageable behavior of SMC composites [18,20,31], we choose a modular anisotropic damage model which is formulated in the setting of generalized standard materials [69] and utilizes a convex dissipation potential [70,71]. This framework relies upon modular damage-activation functions and stress extraction tensors, fulfills Wulfinghoff's damage growth criterion [72] and ensures a well-posed model precluding localization. We provide an overview of the model and the associated set of parameters in Section 3. To capture the anisotropic damage in the SMC composite fiber bundles, we develop a set of extraction tensors motivated by Puck's theory [73,74] and maximum stress states. To model the UPPH matrix behavior, we introduce an extraction tensor accounting for damage due to dilatation.

We identify all associated damage parameters via a Bayesian optimization approach with Gaussian regression, as presented in Section 4. Using an anisotropic kernel function and parallel executions of FFT-based full-field computational homogenization [56] simulations, we are able to unambiguously identify damage parameter sets for the SMC composite in Section 5.

In Section 6, we analyze our full-field damage predictions and compare the results with μCT scans provided by Schöttl et al. [25,26]. Furthermore, we compute three-dimensional, effective failure surfaces for the SMC composite, using failure criteria based on failure distributions evaluated in the experimental investigations, see Section 2. Hence, we provide both full-field damage evolution in SMC composites on the microscale as well as macroscopic failure surfaces for different failure criteria taking the anisotropic and heterogeneous microstructure of SMC composites into account. These micromechanics-based failure surfaces are formulated in stress space to be used in a structural analysis [15], as well as via residual stiffnesses to be used in a design (optimization) process [75]. Our presented multiscale approach helps paving the way for an application-based anisotropic damage and failure evaluation of SMC composites on component scale level.

1.3. Notation

We follow a direct tensor notation throughout this work. We denote vectors and second-order tensors by lower case and upper case bold letters, respectively (e. g., $\boldsymbol{a}$ and $\boldsymbol{A}$), and fourth-order tensors by, e. g., $\mathbb{A}, \mathbb{B}$. The transposition of a vector and second-order tensor reads $\boldsymbol{a}^{\mathsf{T}}$ and $\boldsymbol{A}^{\mathsf{T}}$. We denote the linear mappings induced by second-order and fourth-order tensors as $\boldsymbol{a} = \boldsymbol{C}\boldsymbol{b}$ and $\boldsymbol{A} = \mathbb{C}[\boldsymbol{B}]$, respectively. We write the composition of two second-order or two fourth-order tensors by $\boldsymbol{A}\boldsymbol{B}$ and $\mathbb{A}\mathbb{B}$, and the Frobenius inner product by $\boldsymbol{A} \cdot \boldsymbol{B} = \mathrm{tr}(\boldsymbol{A}\boldsymbol{B}^{\mathsf{T}})$. The tensor product is symbolized by $\otimes$ and its symmetrized version $\otimes_{\mathrm{S}}$ is defined via $\boldsymbol{a} \otimes_{\mathrm{S}} \boldsymbol{b} = (\boldsymbol{a} \otimes \boldsymbol{b} + \boldsymbol{b} \otimes \boldsymbol{a})/2$. We use the abbreviation $\boldsymbol{a}^{\otimes n} = \boldsymbol{a} \otimes \boldsymbol{a} \cdots \otimes \boldsymbol{a}$ (n repetitions of $\boldsymbol{a}$). The material time derivative of a quantity w is expressed as $\dot{w} = \mathrm{D}w/\mathrm{D}t$. The unit sphere in $\mathbb{R}^3$ reads S^2. Generally, we use a $\{\boldsymbol{e}_1, \boldsymbol{e}_2, \boldsymbol{e}_3\}$ Cartesian coordinate system on the (local) microscale and a $\{\boldsymbol{e}_x, \boldsymbol{e}_y, \boldsymbol{e}_z\}$ Cartesian coordinate system on the (effective) macroscale. Details on further spaces of interest, domains of definition and corresponding explicit expressions are given upon their first appearance.

2. Sheet molding compound (SMC) composites

2.1. Microstructure of SMC composites

We consider an SMC composite comprised of an unsaturated polyester polyurethane hybrid (UPPH) resin [3], reinforced by glass fibers. The SMC composite is specifically designed to be used for the manufacturing of structural, load-bearing components. The matrix was developed to possess a stable bi-stage state allowing for a co-molding of glass and carbon fibers [13]. No fillers are added to the composite. The compression molding process leads to a fiber bundle microstructure of the SMC composite [1,76,77], where each bundle of fibers remains intact with an approximately unidirectional orientation of the fibers within a bundle. Dedicated algorithms [9,25,78] reveal the fiber bundle structure on μCT images, see Fig. 1. Similar microstructure characteristics are observed for mesostructure analysis via optical microscopy on polished SMC composite sample surfaces [19,79] and accounted for in hierarchical approaches [11,20].

The linear elastic properties of the UPPH matrix and fibers are listed in Table 1. To derive the properties of a fiber bundle, we implemented two different approaches, numerical full-field homogenization of a representative bundle [80], as well as mean-field Mori–Tanaka homogenization [51,54]. Both approaches lead to approximately the same transversely isotropic stiffness properties that are listed in Table 1, where "L" and "T" refer to longitudinal and transverse, respectively. Measurements and comparisons of the effective elastic properties of SMC composites were performed by Trauth et al. [12].

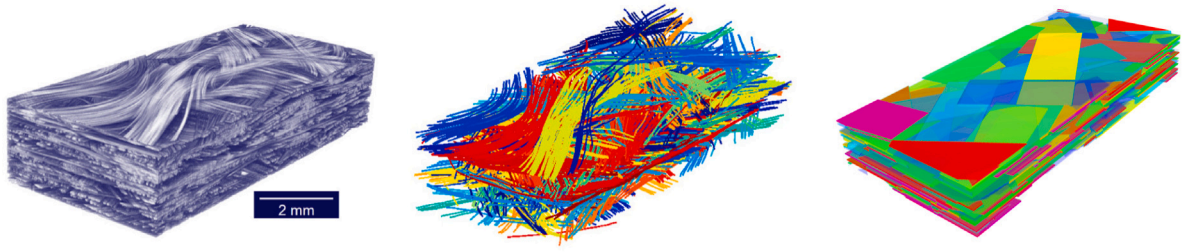

(a) Volumetric µCT image [9] (b) Identified fiber bundles [9] (c) Generated microstructure [58]

Fig. 1. Real fiber bundle microstructure of an SMC composite as investigated by Schöttl et al. [9,25] and generated microstructure [58].

Table 1
Material properties for the considered SMC composite.

E-glass fibers [22]	UPPH matrix [22]	Fiber bundles [58]
$E_{\mathrm{F,iso}} = 72$ GPa	$E_{\mathrm{M,iso}} = 3.4$ GPa	$E_{\mathrm{B,L}} = 37.73$ GPa $E_{\mathrm{B,T}} = 10.33$ GPa
$\nu_{\mathrm{F,iso}} = 0.22$	$\nu_{\mathrm{M,iso}} = 0.385$	$\nu_{\mathrm{B,TT}} = 0.477$ $\nu_{\mathrm{B,LT}} = 0.292$
$G_{\mathrm{F,iso}} = 29.51$ GPa	$G_{\mathrm{M,iso}} = 1.23$ GPa	$G_{\mathrm{B,TT}} = 3.58$ GPa $G_{\mathrm{B,LT}} = 3.64$ GPa

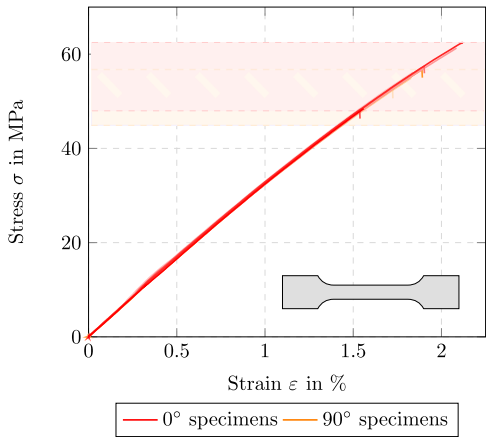

Fig. 2. Neat UPPH bone specimens loaded in different directions (with courtesy of M. Bartkowiak and A. Trauth, Institute for Applied Materials – Materials Science and Engineering) in analogy to investigations by Kehrer et al. [22].

2.2. Experimental investigations

2.2.1. Neat UPPH

Specimens oriented in different directions were cut from manufactured neat UPPH sheets and tested uniaxially. The resulting stress–strain curves, as well as the shape of the specimens, are shown in Fig. 2. The measured Young's moduli, according to DIN EN ISO 527-4 [81], coincide with the Young's moduli measured by Kehrer et al. [22], as shown in the histogram Fig. 3(a). The computed mean value for the considered experiments is 3.38 GPa with a standard deviation of 0.06 GPa. Furthermore, the non-linear regime up to failure is visible. As the structural behavior of the different specimens cannot be distinguished, it is reasonable to use an isotropic model for UPPH. The ultimate strength, i. e., the stress at failure, has an average value of 52.6 MPa with a standard deviation of 5.5 MPa, see Fig. 3(b). The bandwidth of values for the ultimate strength, also accounting for the different orientations, are highlighted as horizontal coloring in Fig. 2. Assuming a pure elasto-damageable behavior, we determined the Young's moduli at failure as a measure of stiffness reduction (or damage evolution) via $\Delta\sigma/\Delta\varepsilon$, see Fig. 3(c). The mean of all Young's moduli at failure is 3.01 GPa with a standard deviation of 0.08 GPa. Relating the Young's moduli at failure to the corresponding initial Young's moduli we get the stiffness reduction shown in Fig. 3(d). On average, this reduction is 10.67% with a standard deviation of 3.19%.

2.2.2. SMC composite

For our SMC composite, we follow a similar procedure to the investigations on neat UPPH specimens. Based on previously conducted experimental investigations in terms of dynamic mechanical analysis [22,82], as well as loading and unloading scenarios, conceivably coupled to acoustic emission analysis [12,18,77], we know damage to be the predominant mechanism in the considered high performance SMC composite. Hence, we neglect viscous and plastic effects and focus on the analysis of uniaxial tensile tests to evaluate the onset of damage. Therefore, specimens with different orientations were cut from manufactured SMC composite sheets with a fiber volume fraction of 25%. These sheets were produced in a two-dimensional compression molding flow-process where the bi-staged sheets are placed in the middle of the tool. Four different specimen geometries were used, see Fig. 4 – two rectangular specimens (types A and B) and two bone specimens (types C and D) with widths of 15 mm and 30 mm, respectively.

Fig. 5(a) shows the measured Young's moduli corresponding to the stress–strain curves in Fig. 4. These Young's moduli have a mean of 11.85 GPa with a standard deviation of 1.92 GPa, and confirm the moduli measured by Trauth, Kehrer and co-workers [18,22]. The measured ultimate strength has a mean of 144.78 MPa and a standard deviation of 15.15 MPa, as shown in Fig. 5(b). The total bandwidth of the ultimate strength is highlighted in Fig. 4. The histogram and normal distribution of the damaged (reduced) Young's moduli at failure are shown in Fig. 5(c). On average, the damaged Young's moduli take a value of 8.85 GPa with a standard deviation of 0.94 GPa. The average stiffness reduction at failure is 23.67% with a standard deviation of 12.79%, as shown in Fig. 5(d).

2.2.3. In-situ µCT scan analysis

In addition to pre-processing μCT scans on unscathed specimens, also in-situ μCT scans were performed by Schöttl et al. [25,26]. Snapshots of a specimen loaded vertically in such an in-situ experiment, aiming mainly at damage evolution and microcrack segmentation, are shown in Fig. 6. The characteristic fiber bundle microstructure is clearly visible in the μCT scan shown in Fig. 6(a). Cyclic loading with increased loading steps and in-between holding times for μCT scan analysis evoke a relatively stable damage evolution within the material due to microcrack propagation and hence allow for damage detection via scanning [25]. The investigations show matrix damage perpendicular to the loading direction to be the primary damage mechanism [18,25]. Microcracks initiate at rims of matrix-rich areas – mainly at the edge or at fiber bundle interfaces – and progress through the material, diverted by bundles [26]. Depending on the orientation of individual bundles and hence the associated local stress state, microcracks either follow the principal bundle direction or run through it. Increasing the loading level leads to a higher microcrack density and a wider spread, until eventually total macroscopic failure is inevitable, see Figs. 6(c) and 6(d). Fiber or bundle breakage is hardly observed and partially occurs at the point of macroscopic failure [40,83].

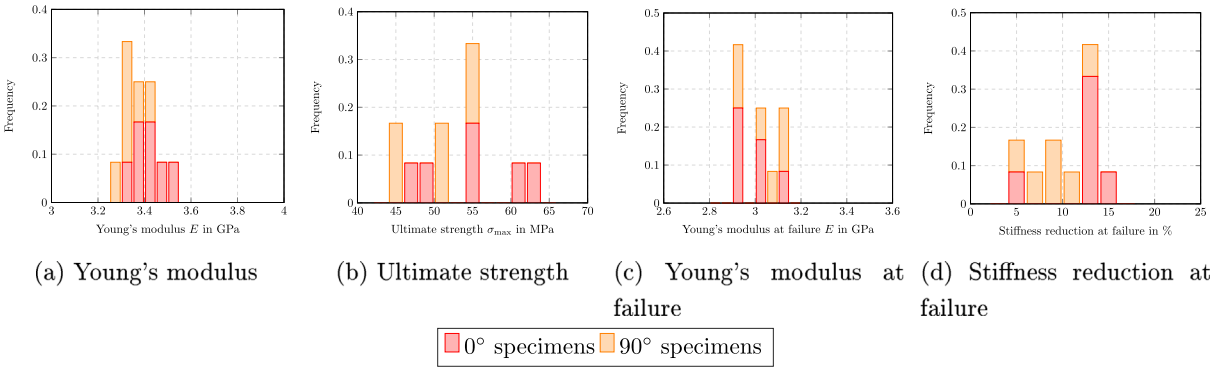

Fig. 3. Analysis of the neat UPPH bone specimens shown in Fig. 2.

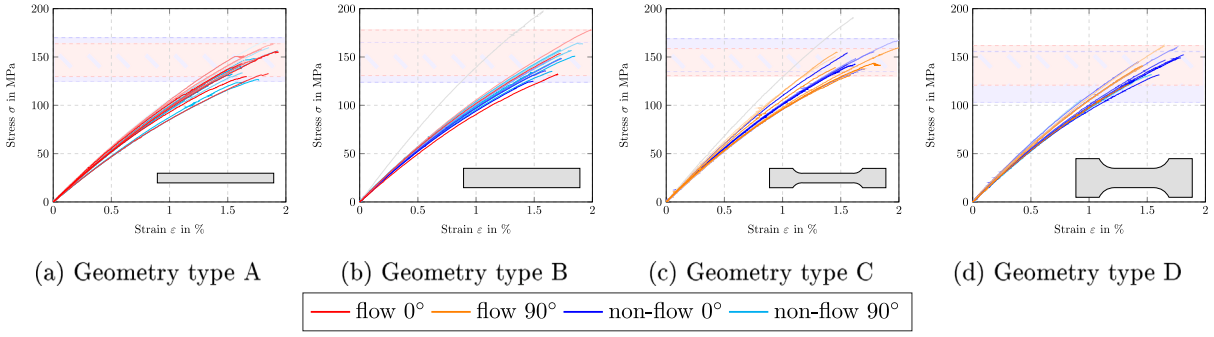

Fig. 4. SMC composite specimens of different geometry types, loaded in different directions, investigated by Trauth, Bartkowiak and co-workers [12,18].

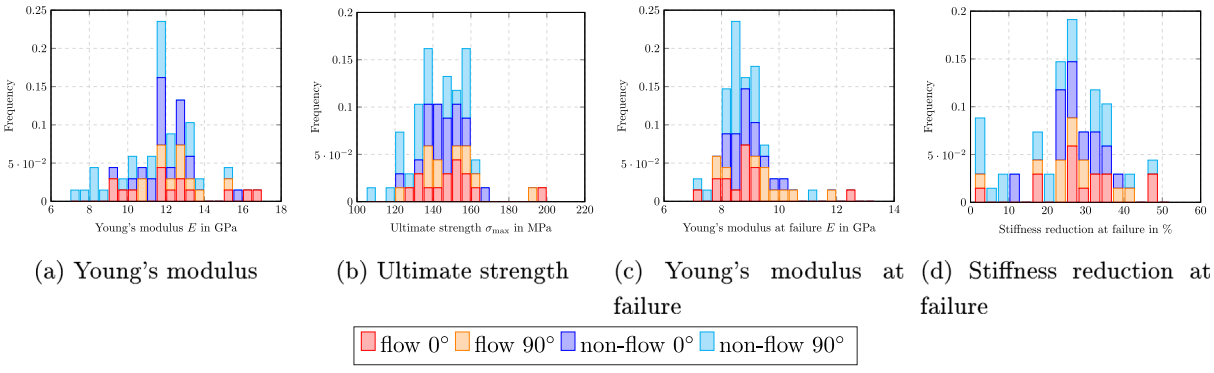

Fig. 5. Analysis of the SMC composite specimens shown in Fig. 4.

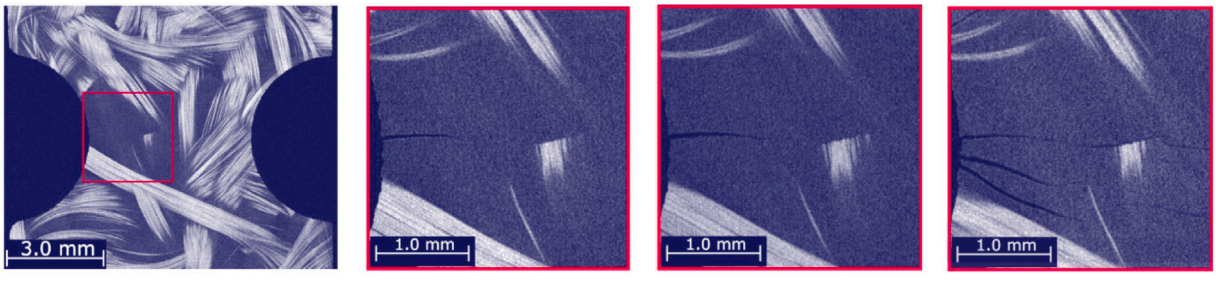

Fig. 6. Snapshots of an in-situ SMC composite specimen for different loading steps in vertical direction showing the evolution of microcracks, as investigated by Schöttl et al. [25,26]. All shown snapshots are published under CC BY 4.0 license in [26].

3. A modular framework to describe anisotropic damage based on extraction tensors

3.1. A compliance-based anisotropic damage model

To describe damage evolution within the SMC composite, we implement a corresponding model [69] formulated in the framework of generalized standard materials (GSM) [70]. The modular nature of the model allows for an effortless employment to describe both damage within the matrix and the fiber bundles, based on associated extraction tensors. In the following, we briefly recall the most important aspects of the damage model [69].

The first potential in the GSM framework is the free energy in terms of a Hookean elastic energy and an energy related to the progressive damage

$$w : \mathrm{Sym}(d) \times S_d \times \mathbb{R}^M \to \mathbb{R}, \quad (\boldsymbol{\varepsilon}, \mathbb{S}, q) \mapsto \frac{1}{2}\, \boldsymbol{\varepsilon} \cdot \mathbb{S}^{-1}[\boldsymbol{\varepsilon}] + \sum_{i=1}^{M} \frac{H_i}{m_i + 1} q_i^{m_i+1}, \quad m_i > 0. \tag{3.1}$$

The former is jointly convex in the strain $\boldsymbol{\varepsilon}$ and the compliance $\mathbb{S}$ and infinitely often differentiable. The latter is introduced as a power-law hardening type in terms of M different damage variables q_i, hardening parameters H_i and exponents m_i and hence is convex and continuously differentiable. The space of symmetric $d \times d$ infinitesimal strain tensors $\boldsymbol{\varepsilon}$ is $\mathrm{Sym}(d)$ (with d being the dimension, i. e., $d \in [2, 3]$), the compliance tensors are $\mathbb{S} \in S_d = \{\mathbb{S} \in \mathrm{Sym}(\mathrm{Sym}(d)) \,|\, \boldsymbol{\tau} \cdot \mathbb{S}[\boldsymbol{\tau}] > 0 \text{ for all } \boldsymbol{\tau} \in \mathrm{Sym}(d) \backslash \{0\}\}$, and the damage variables $q \in \mathbb{R}^M$ are M scalars in real space. A more detailed discussion can be found in [69].

The second potential in the GSM framework is the force potential

$$\boldsymbol{\Phi}^*(\mathbb{T}, \beta) = \begin{cases} 0, & \phi_i(\mathbb{T}, \beta) \le 0 \quad \text{for all} \quad i = 1, \dots, M, \\ +\infty, & \text{otherwise}, \end{cases} \tag{3.2}$$

which we introduce via M convex and continuously differentiable damage-activation functions

$$\phi_i : \mathrm{Sym}(\mathrm{Sym}(d)) \times \mathbb{R} \to \mathbb{R}, \quad (\mathbb{T}, \beta_i) \mapsto 2\mathbb{T} \cdot \mathbb{B}_i^2 - \sigma_{0,i}^2 + H_i \beta_i, \quad i = 1, \dots, M. \tag{3.3}$$

Each damage-activation function is formulated in terms of the conjugate driving forces $\mathbb{T} \in \mathrm{Sym}(\mathrm{Sym}(d))$ for the compliance and $\beta_i \in \mathbb{R}$ for the damage variables, respectively. Furthermore, a fourth-order extraction tensor $\mathbb{B}_i \in L(\mathrm{Sym}(d))$ and a damage-activation threshold $\sigma_{0,i}$ are introduced per damage-activation function ϕ_i. As the driving forces are given by their potential-based relations $\mathbb{T} = \frac{1}{2}\boldsymbol{\sigma} \otimes \boldsymbol{\sigma}$ and $\beta_i = -H_i q_i^{m_i}$, we simplify the damage-activation functions ϕ_i in terms of the stress $\boldsymbol{\sigma}$ and the damage variables q_i as

$$f_i : \mathrm{Sym}(d) \times \mathbb{R} \to \mathbb{R}, \quad (\boldsymbol{\sigma}, q_i) \mapsto \|\mathbb{B}_i[\boldsymbol{\sigma}]\|^2 - \sigma_{0,i}^2 - H_i^2 q_i^{m_i}, \quad i = 1, \dots, M. \tag{3.4}$$

Biot's dual equation [84] in the context of the introduced potentials (3.1) and (3.2) yields the evolution equations for the internal variables $\mathbb{S}$ and q, where the consistency parameters need to obey the classical Karush–Kuhn–Tucker (KKT) conditions [85,86]. With a little work, we eliminate the consistency parameters and reformulate the equations, s. t. we compute the compliance at time t as

$$\mathbb{S}(t) = \mathbb{S}_0 + 2 \sum_{i=1}^{M} \frac{q_i(t)}{H_i} \mathbb{B}_i^2, \tag{3.5}$$

where $\mathbb{S}_0 = \mathbb{S}(0)$ is the initial compliance. The associated KKT conditions referring to the simplified damage-activation functions f_i and damage variables q_i read

$$f_i(\boldsymbol{\sigma}, q_i) \le 0, \quad \dot{q}_i \ge 0, \quad \dot{q}_i\, f_i(\boldsymbol{\sigma}, q_i) = 0, \quad i = 1, \dots, M. \tag{3.6}$$

3.2. Influence of the model parameters

The model is able to describe progressive, fully anisotropic damage of any (anisotropic) initial stiffness $\mathbb{C}_0 = \mathbb{S}_0^{-1}$ via any number of damage-activation functions (3.4). Each damage-activation function f_i involves three parameters, a damage-activation threshold $\sigma_{0,i}$, a hardening parameter H_i and a power-law exponent m_i. As the squared norm of the extracted stress $\|\mathbb{B}_i[\boldsymbol{\sigma}]\|^2$ reaches $\sigma_{0,i}^2$, damage evolution is triggered, and the damage variable q_i increases. The damage evolution and hence the non-linear hardening-type stress–strain relation are governed by H_i and m_i. The influence of the parameters on the predicted stress–strain relations is shown in Fig. 7 as an example. Here, a single damage-activation function f to describe damage in loading direction, in analogy to Govindjee et al. [87], is used. We choose the set of damage parameters as $\sigma_0 = 30$ MPa, $H = 130$ MPa and $m = 1$ for reference. For each study shown in Fig. 7, we vary one of these parameters and keep the others constant.

Increasing the damage-activation threshold σ_0 retards the damage initiation and increases the elastic region, see Fig. 7(a). The hardening parameter H and the power-law exponent m have an opposing influence on the damage region, as we observe when comparing Figs. 7(b) and 7(c). Whereas an increase of H increases the hardening-type behavior, an increase of m decreases the hardening.

3.3. Extraction tensors accounting for dilatation and distortion

3.3.1. Spherical stress state

To model damage induced by dilatation, i. e. due to spherical stress states, the corresponding extraction tensor $\mathbb{B}$ is the spherical projector $\mathbb{P}_1$, well-known from linear elasticity

$$\mathbb{B} = \mathbb{P}_1 = \frac{1}{3}\boldsymbol{I} \otimes \boldsymbol{I}. \tag{3.7}$$

Due to its characteristic $\mathbb{P}_1[\boldsymbol{\sigma}] = \boldsymbol{\sigma}^\circ$, the extracted stresses of the defined damage-activation functions (3.4) read

$$\|\mathbb{B}[\boldsymbol{\sigma}]\|^2 = \|\boldsymbol{\sigma}^\circ\|^2. \tag{3.8}$$

3.3.2. Deviatoric stress state

In analogy to spherical stress states, we model damage induced by distortion, i. e. by deviatoric stress states, via an extraction tensor $\mathbb{B}$ of the form

$$\mathbb{B} = \mathbb{P}_2 = \mathbb{I}^{\mathrm{S}} - \mathbb{P}_1. \tag{3.9}$$

Due to the characteristic of the deviatoric projector $\mathbb{P}_2[\boldsymbol{\sigma}] = \boldsymbol{\sigma}'$, the corresponding extracted stresses are

$$\|\mathbb{B}[\boldsymbol{\sigma}]\|^2 = \|\boldsymbol{\sigma}'\|^2. \tag{3.10}$$

3.4. Puck-type extraction tensors accounting for maximum stresses

3.4.1. Basic idea

Motivated by the basic stress states present in laminates, as investigated by Puck et al. [73,74], we define extraction tensors to account for damage due to normal as well as shear loading, both in fiber bundle direction and perpendicular to it. Let $\{\boldsymbol{e}_1, \boldsymbol{e}_2, \boldsymbol{e}_3\}$ be a Cartesian coordinate system, where $\boldsymbol{e}_1$ corresponds to the alignment direction of the fibers, see Fig. 8. Then the stress tensor $\boldsymbol{\sigma}$ admits the block decomposition

$$\boldsymbol{\sigma} = \left(\begin{array}{c|cc} \sigma_{11} & \sigma_{12} & \sigma_{13} \\ \hline \sigma_{12} & \sigma_{22} & \sigma_{23} \\ \sigma_{13} & \sigma_{23} & \sigma_{33} \end{array}\right). \tag{3.11}$$

The stress in fiber direction is given by σ_{11}, the lower right block describes the transverse stresses in the plane orthogonal to the fiber direction, and $(\sigma_{12}, \sigma_{13})$ are the remaining shear stresses in longitudinal fiber bundle direction. Given the basic stress state in a fiber bundle (see

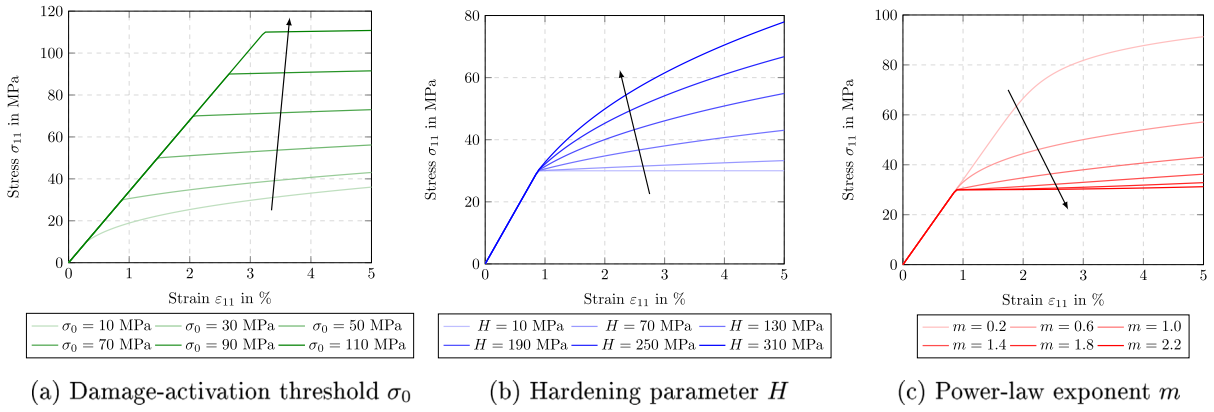

(a) Damage-activation threshold σ_0 (b) Hardening parameter H (c) Power-law exponent m

Fig. 7. Influence of the model parameters σ_0, H and m on the predicted stress–strain relation.

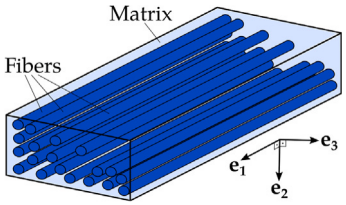

Fig. 8. Schematic of a fiber bundle with local coordinate system $\{\boldsymbol{e}_1, \boldsymbol{e}_2, \boldsymbol{e}_3\}$.

Eq. (3.11)), the traction vector $\boldsymbol{t}$ in an arbitrary direction $\boldsymbol{n}$ is $\boldsymbol{t} = \boldsymbol{\sigma n}$. To account for the maximum stresses in terms of a Puck-type setting, we need to maximize specific (extracted) stresses over certain directions using the pencil-glide approach [88,89]. We distinguish four different loading scenarios that yield four associated extraction tensors.

3.4.2. Normal loading in fiber direction

The traction vector pointing in fiber direction $\boldsymbol{e}_1$ is

$$\boldsymbol{t}_1 = \left(\boldsymbol{e}_1 \cdot \boldsymbol{\sigma e}_1\right) \boldsymbol{e}_1, \tag{3.12}$$

with the scalar stress

$$t_1 = \boldsymbol{e}_1 \cdot \boldsymbol{\sigma e}_1 = \sigma_{11}. \tag{3.13}$$

This stress is unambiguously defined by the given bundle direction $\boldsymbol{e}_1$. The extraction tensor capturing normal loading in fiber direction is

$$\mathbb{B} = \boldsymbol{e}_1^{\otimes 4}. \tag{3.14}$$

Accordingly, the extracted stress reads

$$\|\mathbb{B}\,[\boldsymbol{\sigma}]\,\|^2 = \sigma_{11}^2. \tag{3.15}$$

3.4.3. Normal loading perpendicular to fiber direction

An arbitrary traction vector perpendicular to the fiber direction is given via the direction $S^2 \ni \boldsymbol{k} \perp \boldsymbol{e}_1$, where $S^2 = \{\boldsymbol{x} \in \mathbb{R}^3 \mid \|\boldsymbol{x}\| = 1\}$, as

$$\boldsymbol{t}_\sigma = (\boldsymbol{k} \cdot \boldsymbol{\sigma k})\, \boldsymbol{k}. \tag{3.16}$$

We need to maximize the normal stress pointing into direction $\boldsymbol{k}$

$$t_\sigma = \boldsymbol{k} \cdot \boldsymbol{\sigma k}, \tag{3.17}$$

over all admissible directions

$$t_\sigma^{\max} = \max_{\boldsymbol{k} \perp \boldsymbol{e}_1} \boldsymbol{k} \cdot \boldsymbol{\sigma k}. \tag{3.18}$$

Hence, $t_\sigma^{\max}$ is the maximum principal stress of the stress state on the $\boldsymbol{e}_1$-plane. This stress state is described by

$$\boldsymbol{\sigma}_\sigma = \sigma_{ij} \boldsymbol{e}_i \otimes \boldsymbol{e}_j, \quad i, j = 2, 3, \tag{3.19}$$

with the corresponding principal stresses

$$\lambda_{2,3} = \frac{\sigma_{22} + \sigma_{33}}{2} \pm \sqrt{\left(\frac{\sigma_{22} - \sigma_{33}}{2}\right)^2 + \sigma_{23}^2}. \tag{3.20}$$

Following the classical convention for principal stresses $\lambda_2 > \lambda_3$, we get

$$t_\sigma^{\max} = \lambda_2. \tag{3.21}$$

We derive the associated extraction tensor and the damage-activation function via the condition

$$\|\mathbb{B}\,[\boldsymbol{\sigma}]\,\|^2 \overset{!}{=} \left(t_\sigma^{\max}\right)^2. \tag{3.22}$$

While this condition (3.22) does not allow for an explicit closed-form description of the associated extraction tensor, the extracted stresses are given via

$$\|\mathbb{B}\,[\boldsymbol{\sigma}]\,\|^2 = \left(\frac{\sigma_{22} + \sigma_{33}}{2} + \sqrt{\left(\frac{\sigma_{22} - \sigma_{33}}{2}\right)^2 + \sigma_{23}^2}\right)^2. \tag{3.23}$$

Based on the procedures and results for the alternate loading scenarios (see Sections 3.4.4 and 3.4.5), as well as extraction tensors formulated in an average stress manner [69], we postulate a damage extraction tensor for normal loading perpendicular to the fiber direction of the form

$$\mathbb{B} = \frac{\sqrt{2}}{2}\left(\boldsymbol{e}_2^{\otimes 2} + \boldsymbol{e}_3^{\otimes 2}\right)^{\otimes 2} + \frac{\sqrt{2}}{4}\left(\boldsymbol{e}_2^{\otimes 2} - \boldsymbol{e}_3^{\otimes 2}\right)^{\otimes 2} + \left(\boldsymbol{e}_2 \otimes_{\mathrm{S}} \boldsymbol{e}_3\right)^{\otimes 2}. \tag{3.24}$$

The associated extracted stress therefore reads

$$\|\mathbb{B}\,[\boldsymbol{\sigma}]\,\|^2 = \frac{1}{4}\left(5\sigma_{22}^2 + 5\sigma_{33}^2 + 6\sigma_{22}\sigma_{33} + 4\sigma_{23}^2\right). \tag{3.25}$$

3.4.4. Shear loading perpendicular to fiber direction

In order to evaluate the stress state due to shear loading perpendicular to the fiber direction, we need to consider the shear part of the traction vector, namely

$$\boldsymbol{t}_\tau = \boldsymbol{\sigma k} - (\boldsymbol{k} \cdot \boldsymbol{\sigma k})\, \boldsymbol{k}. \tag{3.26}$$

We decompose the shear traction vector into shear stresses perpendicular and parallel to the fiber direction

$$\boldsymbol{t}_\tau = \boldsymbol{t}_{\tau\perp} + \boldsymbol{t}_{\tau\parallel}. \tag{3.27}$$

The shear traction vector parallel to the fiber direction is

$$\boldsymbol{t}_{\tau\parallel} = \left(\boldsymbol{e}_1 \cdot \boldsymbol{t}_\tau\right) \boldsymbol{e}_1 = \left(\boldsymbol{e}_1 \cdot \boldsymbol{\sigma k}\right) \boldsymbol{e}_1, \tag{3.28}$$

and, analogously, the shear traction vector perpendicular to the fiber direction is

$$\boldsymbol{t}_{\tau\perp} = \boldsymbol{\sigma k} - \underbrace{(\boldsymbol{k} \cdot \boldsymbol{\sigma k})\, \boldsymbol{k}}_{\boldsymbol{t}_\sigma} - \underbrace{\left(\boldsymbol{e}_1 \cdot \boldsymbol{\sigma k}\right) \boldsymbol{e}_1}_{\boldsymbol{t}_{\tau\parallel}}$$

$$= \left(\boldsymbol{I} - \boldsymbol{k}\otimes\boldsymbol{k} - \boldsymbol{e}_1\otimes\boldsymbol{e}_1\right)\boldsymbol{\sigma}\boldsymbol{k} \tag{3.29}$$

$$= (\boldsymbol{m}\cdot\boldsymbol{\sigma}\boldsymbol{k})\,\boldsymbol{m}, \tag{3.30}$$

where $S^2 \ni \boldsymbol{m} \perp \boldsymbol{k} \perp \boldsymbol{e}_1$ and $\boldsymbol{m} \perp \boldsymbol{e}_1$. The sought scalar shear stress is given as

$$t_{\tau\perp} = \boldsymbol{m}\cdot\boldsymbol{\sigma}\boldsymbol{k}, \tag{3.31}$$

which we need to maximize over all admissible directions $\boldsymbol{m} \perp \boldsymbol{k} \perp \boldsymbol{e}_1$

$$t_{\tau\perp}^{\max} = \max_{\boldsymbol{m}\perp\boldsymbol{k}\perp\boldsymbol{e}_1} \boldsymbol{m}\cdot\boldsymbol{\sigma}\boldsymbol{k}. \tag{3.32}$$

Note that the directions $\boldsymbol{m}$ and $\boldsymbol{k}$ are not independent. For a given bundle direction $\boldsymbol{e}_1$, we express $\boldsymbol{m}$ as a function of $\boldsymbol{k}$ via the condition $\boldsymbol{I} = \boldsymbol{m}\otimes\boldsymbol{m} + \boldsymbol{k}\otimes\boldsymbol{k} + \boldsymbol{e}_1\otimes\boldsymbol{e}_1$. Using this relation we get the expression

$$t_{\tau\perp}^{\max} = \max_{\boldsymbol{k}\perp\boldsymbol{e}_1} \sqrt{\|\boldsymbol{\sigma}\boldsymbol{k}\|^2 - (\boldsymbol{k}\cdot\boldsymbol{\sigma}\boldsymbol{k})^2 - \left(\boldsymbol{e}_1\cdot\boldsymbol{\sigma}\boldsymbol{k}\right)^2}, \tag{3.33}$$

involving only a single unknown unit vector $\boldsymbol{k}$. Analogously to normal loading perpendicular to the fiber direction, $t_{\tau\perp}^{\max}$ is the maximum shear stress on the plane defined by the bundle direction $\boldsymbol{e}_1$. In accordance with principal stresses computed for the case above, the maximum shear stress is

$$t_{\tau\perp}^{\max} = \frac{|\lambda_2 - \lambda_3|}{2} = \sqrt{\left(\frac{\sigma_{22}-\sigma_{33}}{2}\right)^2 + \sigma_{23}^2}. \tag{3.34}$$

The associated extraction tensor and the damage-activation function are computed via the condition

$$\|\mathbb{B}\,[\boldsymbol{\sigma}]\,\|^2 \overset{!}{=} \left(t_{\tau\perp}^{\max}\right)^2, \tag{3.35}$$

which is ensured, provided

$$\mathbb{B}^2\,[\boldsymbol{\sigma}] \overset{!}{=} \frac{\sigma_{22}-\sigma_{33}}{4}\left(\boldsymbol{e}_2^{\otimes 2} - \boldsymbol{e}_3^{\otimes 2}\right) + \sigma_{23}\left(\boldsymbol{e}_2 \otimes_{\mathrm{S}} \boldsymbol{e}_3\right) \tag{3.36}$$

holds. Evaluating this condition yields an explicit form of the extraction tensor

$$\mathbb{B} = \frac{\sqrt{2}}{4}\left(\boldsymbol{e}_2^{\otimes 2} - \boldsymbol{e}_3^{\otimes 2}\right)^{\otimes 2} + \left(\boldsymbol{e}_2 \otimes_{\mathrm{S}} \boldsymbol{e}_3\right)^{\otimes 2}, \tag{3.37}$$

and the corresponding extracted stress

$$\|\mathbb{B}\,[\boldsymbol{\sigma}]\,\|^2 = \frac{1}{4}\left(\sigma_{22}^2 + \sigma_{33}^2 - 2\sigma_{22}\sigma_{33} + 4\sigma_{23}^2\right). \tag{3.38}$$

3.4.5. Shear loading in fiber direction

We account for the maximum stress due to shear loading in fiber direction via the corresponding shear traction vector (3.28)

$$\boldsymbol{t}_{\tau\parallel} = \left(\boldsymbol{e}_1\cdot\boldsymbol{\sigma}\boldsymbol{k}\right)\boldsymbol{e}_1 = t_{\tau\parallel}\boldsymbol{e}_1. \tag{3.39}$$

We maximize the associated shear stress over all admissible directions $\boldsymbol{k} \perp \boldsymbol{e}_1$

$$t_{\tau\parallel}^{\max} = \max_{\boldsymbol{k}\perp\boldsymbol{e}_1} \boldsymbol{e}_1\cdot\boldsymbol{\sigma}\boldsymbol{k}, \tag{3.40}$$

i. e. we search the normal direction $\boldsymbol{k}$ that points into direction of the maximum stress [88,89]. As the stress is symmetric $\boldsymbol{\sigma}^{\mathsf{T}} = \boldsymbol{\sigma}$, the relation

$$t_{\tau\parallel} = \boldsymbol{e}_1\cdot\boldsymbol{\sigma}\boldsymbol{k} = \boldsymbol{k}\cdot\boldsymbol{\sigma}\boldsymbol{e}_1 \tag{3.41}$$

holds. We define a corresponding projector $\boldsymbol{P}_k$ with the characteristics $\boldsymbol{P}_k\boldsymbol{k} = \boldsymbol{k}$ and $\boldsymbol{P}_k^{\mathsf{T}} = \boldsymbol{P}_k$ as

$$\boldsymbol{P}_k = \boldsymbol{I} - \boldsymbol{e}_1\otimes\boldsymbol{e}_1. \tag{3.42}$$

Application of this projector to the stress state yields

$$t_{\tau\parallel} = \boldsymbol{k}\cdot\boldsymbol{\sigma}\boldsymbol{e}_1 = \boldsymbol{P}_k\boldsymbol{k}\cdot\boldsymbol{\sigma}\boldsymbol{e}_1 = \boldsymbol{k}\cdot\boldsymbol{P}_k\boldsymbol{\sigma}\boldsymbol{e}_1 = \boldsymbol{k}\cdot\left(\sigma_{12}\boldsymbol{e}_2 + \sigma_{13}\boldsymbol{e}_3\right). \tag{3.43}$$

The shear stress is maximized whenever

$$\boldsymbol{k} \overset{!}{=} \frac{\boldsymbol{P}_k\boldsymbol{\sigma}\boldsymbol{e}_1}{\|\boldsymbol{P}_k\boldsymbol{\sigma}\boldsymbol{e}_1\|} \tag{3.44}$$

holds, yielding

$$t_{\tau\parallel}^{\max} = \frac{\boldsymbol{P}_k\boldsymbol{\sigma}\boldsymbol{e}_1}{\|\boldsymbol{P}_k\boldsymbol{\sigma}\boldsymbol{e}_1\|}\cdot\boldsymbol{P}_k\boldsymbol{\sigma}\boldsymbol{e}_1 = \|\boldsymbol{P}_k\boldsymbol{\sigma}\boldsymbol{e}_1\| = \sqrt{\sigma_{12}^2 + \sigma_{13}^2}. \tag{3.45}$$

The essential relation

$$\|\mathbb{B}\,[\boldsymbol{\sigma}]\,\|^2 \overset{!}{=} \left(t_{\tau\parallel}^{\max}\right)^2, \tag{3.46}$$

holds, if

$$\mathbb{B}^2\,[\boldsymbol{\sigma}] \overset{!}{=} \sigma_{12}\left(\boldsymbol{e}_1 \otimes_{\mathrm{S}} \boldsymbol{e}_2\right) + \sigma_{13}\left(\boldsymbol{e}_1 \otimes_{\mathrm{S}} \boldsymbol{e}_3\right). \tag{3.47}$$

Evaluating this relation gives an explicit form for the associated extraction tensor

$$\mathbb{B} = \left(\boldsymbol{e}_1 \otimes_{\mathrm{S}} \boldsymbol{e}_2\right)^{\otimes 2} + \left(\boldsymbol{e}_1 \otimes_{\mathrm{S}} \boldsymbol{e}_3\right)^{\otimes 2}, \tag{3.48}$$

and the corresponding extracted stress

$$\|\mathbb{B}\,[\boldsymbol{\sigma}]\,\|^2 = \sigma_{12}^2 + \sigma_{13}^2. \tag{3.49}$$

4. Bayesian optimization process

The presented framework takes damage parameters into account (see Sections 3.1 and 3.2), which need to be identified to describe the elasto-damageable behavior of our SMC composite properly. The model and its parameters serve as input for the FFT-based full-field homogenization computed with our in-house code `homKIT` (see Fig. 9 and Section 5.1 for further information). The stress–strain response computed by `homKIT` is compared to the experimental results discussed in Section 2.2 via a corresponding error measure, yielding an optimization problem for the identification of proper damage parameters. We choose a Bayesian optimization approach [90,91], as our problem at hand involves an objective function that is expensive to evaluate (each call involves a full-field homogenization on a three-dimensional voxel image) and derivatives that are not easily calculated. Similar conditions hold for, e. g., ductile phase-field fracture [92]. Bayesian optimization uses a surrogate model of the actual problem accounting for probabilities and uncertainties based on Bayesian statistics [93].

We describe the problem in terms of an abstract cost function

$$c : \mathcal{R} \to \mathbb{R}, \quad p \mapsto c(p), \tag{4.1}$$

combining the full-field homogenization based on a parameter set $p \in \mathcal{R} \subset \mathbb{R}^b$, and the error measure. The feasible domain $\mathcal{R}$ for the parameter set p represents the parameter ranges and is frequently chosen as hyper-rectangle with $p \in \mathcal{R} \subset \mathbb{R}^b : l_i \le p_i \le u_i,\ i = 1,\dots,b$, for scalar lower and upper bounds l_i and u_i. We seek a minimizer p of the cost function

$$c(p) \to \min_{p\in\mathcal{R}\subset\mathbb{R}^b}. \tag{4.2}$$

In general, we do not know the (continuous) cost function, but only a certain amount of discrete values for parameter sets $p_{1:r} = \left(p_1,\dots,p_r\right) \in \mathcal{R}^r$, which we assemble in a vector $c_{1:r} = \left[c(p_1),\dots,c(p_r)\right]^{\mathsf{T}} \in \mathbb{R}^r$. The cost function values for the remainder of parameter sets are uncertain, yielding an infinite number of possible cost functions. Hence, we use a surrogate cost function model based on Gaussian process regression [94] to account for the uncertainty within the Bayesian optimization procedure. We assume all possible cost function values to be distributed normally

$$c(p) \sim \mathcal{N}(m(p), K(p,p')) \quad \text{for all} \quad p \in \mathcal{R}, \tag{4.3}$$

with a mean $m : \mathcal{R} \to \mathbb{R}$ and a kernel (covariance) $k : \mathcal{R}\times\mathcal{R} \to \mathbb{R}$. The kernel k defines the correlations of two parameter sets p and p'. Condition (4.3) has to hold for all parameter sets $p \in \mathcal{R}$ yielding a normal distribution of all cost functions. Therefore, given the already known parameter sets $p_{1:r}$ with associated cost function values $c_{1:r}$, all possible (surrogate) cost functions have to be drawn according to the multivariate normal distribution (4.3) with the mean

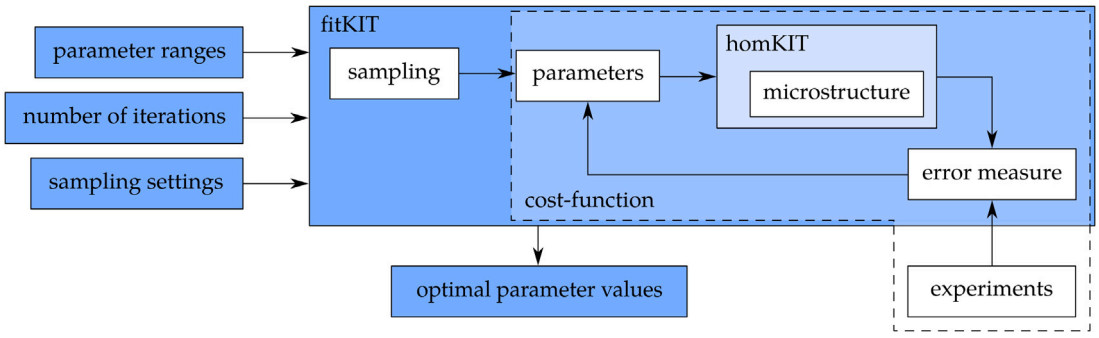

Fig. 9. Simplified schematic workflow of parameter identification routine.

vector $m_{1:r} = \left[m(p_1), \dots, m(p_r)\right]^\mathsf{T} \in \mathbb{R}^r$ and the covariance matrix

$$K_{1:r,1:r} = \begin{bmatrix} k(p_1,p_1) & \dots & k(p_1,p_r) \\ \vdots & \ddots & \vdots \\ k(p_r,p_1) & \dots & k(p_r,p_r) \end{bmatrix} \in \mathbb{R}^{r\times r}. \tag{4.4}$$

The multivariate normal distribution (4.3) has to hold for any new parameter set p_{r+1}, as well. Hence, the joint distribution based on all parameter sets – known and new – $(p_{1:r}, p_{r+1})$ follows a multivariate normal distribution that reads

$$\begin{bmatrix} c_{1:r} \\ c(p_{r+1}) \end{bmatrix} \sim \mathcal{N}\left(0, \begin{bmatrix} K_{1:r,1:r} & K_{1:r,r+1} \\ K_{1:r,r+1}^\mathsf{T} & k(p_{r+1},p_{r+1}) \end{bmatrix}\right), \tag{4.5}$$

with the kernel evaluations $K_{1:r,r+1} = \left[k(p_1,p_{r+1}), \dots, k(p_r,p_{r+1})\right]^\mathsf{T}$ and $k(p_{r+1},p_{r+1})$. For convenience we assume the mean to be zero $m_{1:r} \equiv 0$ [95].

Consequently, the (conditional) posterior probability distribution of the cost function $c(p_{r+1})$ for the new parameter set p_{r+1}, given the already known $c_{1:r}$, is computed as

$$c(p_{r+1}) \mid c_{1:r} = \mathcal{N}\left(\widetilde{m}(p_{r+1}), \widetilde{v}^2(p_{r+1})\right) \tag{4.6}$$

with a posterior mean $\widetilde{m}(p_{r+1})$ and a posterior variance $\widetilde{v}^2(p_{r+1})$. Here, the Sherman–Morrison–Woodbury formula [96] can be utilized [94] and yields

$$\widetilde{m}(p_{r+1}) = K_{1:r,r+1}^\mathsf{T} K_{1:r,1:r}^{-1} c_{1:r}, \tag{4.7}$$

$$\widetilde{v}^2(p_{r+1}) = k(p_{r+1},p_{r+1}) - K_{1:r,r+1}^\mathsf{T} K_{1:r,1:r}^{-1} K_{1:r,r+1}^\mathsf{T}. \tag{4.8}$$

The posterior mean $\widetilde{m}(p_{r+1})$ is estimated on the given, known data $c_{1:r}$ weighted by the kernel. The posterior variance $\widetilde{v}^2(p_{r+1})$ is given by the prior covariance which is corrected by a term that takes the known correlations into account. The posterior mean approximates the actual cost function and is updated and improved with each evaluated parameter set p_{r+1}. For an infinity number of evaluations $r \to \infty$, we recapture the actual (deterministic) cost function.

As we know the different parameters of the different damage-activation functions to have different levels of relevance on the anisotropic behavior of our SMC composite, we use the Màtern 5/2 kernel [97]

$$k(p,p') = \gamma_p^2 \left(1 + \sqrt{5}\,\delta\left(p,p'\right) + \frac{5}{3}\,\delta\left(p,p'\right)^2\right) \exp\left(-\sqrt{5}\,\delta\left(p,p'\right)\right) \tag{4.9}$$

with an anisotropic distance function $\delta\left(p,p'\right)$ between parameter sets p and p'

$$\delta\left(p,p'\right) = \sqrt{\sum_{i=1}^{b} \frac{\left(p_i - p_i'\right)^2}{\alpha_i^2}}. \tag{4.10}$$

The Màtern 5/2 kernel (4.9) is not restricted to smooth cost functions. Each of the hyperparameters $(\alpha_1, \dots, \alpha_b)$ is determined to represent the relevance of its associated damage parameter. The hyperparameter γ_p^2 controls the width of the kernel, i. e., the general level of correlation between two parameter sets. For a more detailed discussion on kernel functions, the reader is referred to the book of Williams and Rasmussen [94].

For each evaluation, we want to choose a new parameter set p_{r+1} that is closer to the sought minimum of the cost function. Hence, a promising parameter set p_{r+1} has a large improvement $\langle c(p_*) - c(p_{r+1})\rangle$ w. r. t. the currently best parameter set $p_* = \text{argmin}_{i\le r} c(p_i)$. As we do not know $c(p_{r+1})$ beforehand, we take the expected value $\mathcal{E}$ of the improvement given all already known evaluations $c_{1:r}$ and maximize it, yielding

$$p_{r+1} = \text{argmax}\, \text{EI}(p), \tag{4.11}$$

with the "expected improvement" (EI) acquisition function [98,99]

$$\text{EI}(p) = \mathcal{E}\left(\langle c(p_*) - c(p)\rangle \mid c_{1:r}\right) \tag{4.12}$$

and Macaulay brackets $\langle\cdot\rangle = \max(0,\cdot)$. We evaluate (4.12) in closed form [99] and arrive at

$$\text{EI}(p) = \langle \vartriangle\, c(p)\rangle + \widetilde{v}(p)\,\text{PDF}\left(\frac{\vartriangle\, c(p)}{\widetilde{v}(p)}\right) - |\vartriangle\, c(p)|\,\text{CDF}\left(\frac{\vartriangle\, c(p)}{\widetilde{v}(p)}\right) \tag{4.13}$$

with the probability and cumulative density functions PDF and CDF. The expected difference is defined as $\vartriangle\, c(p) = c(p_*) - \widetilde{m}(p) - \xi$, including a shift-parameter ξ that helps controlling the exploration and exploitation trade-off [99]. This trade-off between choosing (new) parameter sets with a high uncertainty (high $\widetilde{v}(p)$) or a high expected quality (high $\vartriangle\, c(p)$) is the elementary part of all acquisition functions.

To initialize a certain number of cost function values for the optimization process, we use a Latin-Hypercube sampling approach [100] for the parameter sets within our hyper-rectangular domain $\mathcal{R}$. The Bayesian optimization process is stopped after a given amount of iterations and the parameter set p_* yielding the smallest cost function value $c(p_*)$ is considered as the optimal choice. The variance, or the associated confidence interval, respectively, gives information about quality and certainty of the found optimum.

5. Identification of damage parameters in SMC composites

5.1. Computational setup

We integrated the proposed damage model as a user-defined subroutine in our in-house OpenMP-parallel FFT-based computational homogenization code written in Python 3.7 with Cython extensions [101] and FFTW [102] bindings, as described by Schneider [103] (`homKIT`, see Fig. 9). We use the Moulinec–Suquet discretization [80] and a Newton-CG scheme to solve the ensuing nonlinear systems of equations [104, 105]. We implemented the Bayesian optimization procedure in combination with the kernel evaluations and the error measure in terms of a Python 3.7 code, incorporating GPyOpt [106] (`fitKIT`, see Fig. 9). We executed the optimization iterations in parallel, using a batch sampling as introduced by Thompson [107]. For the computations we used either 6–12 threads on a desktop computer with 32 GB RAM and an Intel i7-8700K CPU with 6 cores and a clock rate of 3.7 GHz, or a workstation with two AMD EPYC 7642 with 48 physical cores each, enabled SMT and 1024 GB of DRAM.

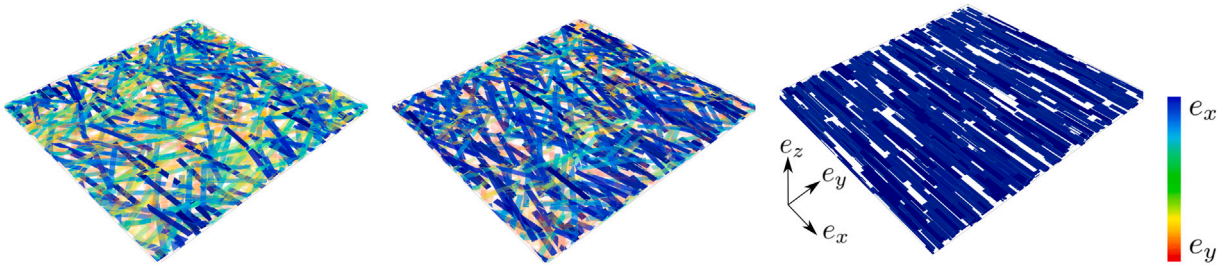

(a) Planar isotropic orientation – diag(0.5, 0.5, 0)

(b) Higher alignment in e_x-direction – diag(0.7, 0.3, 0)

(c) Unidirectional orientation in e_x-direction – diag(1, 0, 0)

Fig. 10. Example of generated unit cells. Coloring indicates bundle orientation. Matrix is hidden.

Table 2
Extraction tensors and parameters used for modeling the behavior of SMC composites.

	Type	$\mathbb{B}$	σ_0 in MPa	H in MPa
UPPH	Section 3.3.1	(3.7)	[5, 50]	[50, 400]
Bundle	Section 3.4.3	(3.24)	[5, 40]	[100, 700]
	Section 3.4.5	(3.48)	[5, 40]	[50, 400]

Table 3
Extraction tensors and identified parameters used to capture the behavior of SMC composites.

	Type	$\mathbb{B}$	σ_0 in MPa	s in %	H in MPa	s in %
UPPH	Section 3.3.1	(3.7)	43.99	24	177.84	3
Bundle	Section 3.4.3	(3.24)	29.36	11	381.64	4
	Section 3.4.5	(3.48)	28.60	51	123.81	7

5.2. Definition of the parameter set to be identified

To capture matrix and bundle damage, the dominant mechanisms in SMC composites [18,20,31], we utilize the following three damage-activation functions (3.4). Matrix damage evolution due to normal loading in terms of dilatation is captured via a damage-activation function in combination with an extraction tensor of type (3.7). Bundle damage in transverse and longitudinal direction, accounting for normal and shear stresses, is described via damage-activation functions in combination with extraction tensors of types (3.24) and (3.48), respectively.

Each damage-activation function comes with three parameters (σ_0, H, m), as discussed in Section 3.2. We know the power-law exponent m to have a contrary influence on the non-linear regime compared to the hardening parameter H. To describe the behavior of SMC composites, we assume a linear damage hardening evolution and hence set the power-law exponent to $m = 1$ for each damage-activation function. This leaves us with six parameters to be identified adequately in order to fit the predicted behavior of our model to the experimental observations. A summary of the applied extraction tensors, the associated parameters and their allowed ranges for the optimization process is given in Table 2.

5.3. Study on SMC composite microstructures

We utilize the Bayesian optimization presented in Section 4 to identify the damage parameters for our SMC composite, see Table 2. We ran our optimization with 300 initial hypercube samplings and subsequent 3000 iterations, computed in 250 batches with 12 parallel executions on 8 threads each. We update the surrogate model and hence the acquisition function after the computation of each batch. The underlying microstructure is a generated unit cell [58], as shown in Fig. 10(a), with a fiber volume fraction of 25% and a planar isotropic orientation, matching the conditions of the specimens discussed in Section 2.2. Using the introduced microstructure generation approach [58], we transfer our results to SMC composite unit cells with different orientations, see Fig. 10 and Section 6. Therefore, we generated additional unit cells with fiber bundles oriented in $\boldsymbol{e}_x$-direction to a higher extent and unit cells with a pure unidirectional bundle alignment in $\boldsymbol{e}_x$-direction, see Figs. 10(b) and 10(c). The associated fiber orientation tensors of second-order [108] are given in the captions.

We use a least square ansatz for the cost function value regarding a parameter set p

$$c(p) = \sqrt{\frac{1}{N}\sum_{i=1}^{N}\left(\sigma_i^{\text{exp}} - \sigma_i^{\text{sim}}(p)\right)^2} \tag{5.1}$$

comparing the difference of the experimentally measured and the predicted stress–strain curves. We evaluate the measures stress σ_i^{exp} and the computed stress $\sigma_i^{\text{sim}}(p)$ for N given strain values. The cost function values $c(p)$ of the 300 initial samples and the best result per batch for the subsequent iterations are shown in Fig. 11. The lighter areas mark the 95% confidence interval for each result. We observe a high variation in the cost function values for the 300 initial sampling iterations, as we raster the complete hyper-rectangular parameter space. In a sense, we maximize the exploitation and minimize the expectation in our discussed trade-off (see Section 4), to gain as much knowledge about the cost function behavior as possible during initialization.

In the following 1400 iterations the variation of the cost function decreases, but nonetheless remains relatively high, see Figs. 11(a) and 11(b). As the behavior of the cost function is governed by six parameters, the individual influences need to be explored, which is responsible for this prolonged variation with its quite large confidence interval. After about a total of 1700 iterations, a possible optimum is found with a cost function value of approximately 0.45 MPa and a small confidence interval of the order of ±0.01 MPa, see Fig. 11(b). For the remainder of the optimization process, the variation of the best cost function value per batch is negligibly small with an associated small confidence interval, see Fig. 11(c). Hence, we can assume the best overall cost function value of about 0.44 MPa (which is 0.33% of the mean ultimate strength) to be reasonably close to the actual optimum. The corresponding values of the best parameter set to describe damage evolution in our SMC composite are listed in Table 3. Furthermore, the sensitivity s of each parameter in terms of its associated hyperparameter related to all hyperparameters is added. In general, the identified optimum of the cost function shows a higher sensitivity w. r. t. the damage-activation threshold σ_0 compared to the hardening parameter H.

A comparison of the experimentally measured stress–strain curve (see Section 2.2, cf. Fig. 4) and the computed stress–strain curve is given in Fig. 12. These curves, representing the macroscopic structural behavior of our SMC composite, are in good agreement. With our defined damage cases, the corresponding damage-activation functions, extraction tensors and identified parameters at hand, we can predict the macroscopic behavior of the SMC composite unit cell accurately.

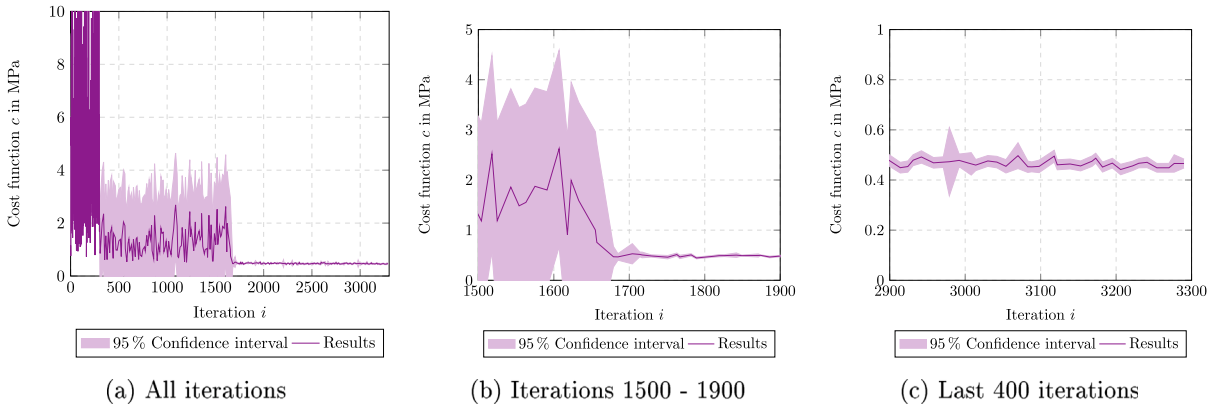

Fig. 11. Best value per batch of the cost function $c(p)$ over iterations.

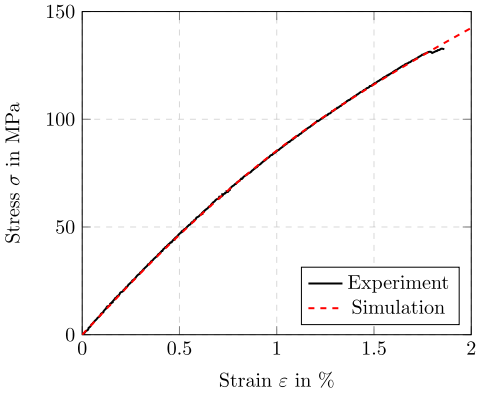

Fig. 12. Comparison of effective stress–strain curves.

6. Identification of macroscopic failure surfaces for SMC composites

6.1. Full-field damage evolution

The introduced damage cases and identified parameters do not only allow for the prediction of the macroscopic stress–strain behavior, but also help us to evaluate the evolution and full-field distribution of damage on the microscale. With damage in terms of microcrack evolution [25,26] in mind, we analyze the predicted damage in the UPPH matrix. The evolution of damage over different loading steps is shown in Fig. 13. In analogy to the discussed experiments, we consider a slice of a planar isotropic microstructure that is loaded in vertical direction. Damage in the matrix mainly initiates at the rims of matrix rich regions at bundle edges and corners, see Figs. 13(a) and 13(b). With increasing loading level, on the one hand the damage level of existing damaged regions increases and expands, and on the other hand additional damaged areas arise, see Figs. 13(c) and 13(d). At a certain loading level, a large share of the matrix is damaged, i. e., the density of microcracks is relatively high, compare Fig. 6(d). Correspondingly, bundle damage evolves as the matrix damage increases. The sum of all these types of damage, matrix damage followed by bundle damage, eventually accumulates to macroscopic failure of the SMC composite. The full-field distribution of bundle damage is discussed in Appendix.

Our presented framework allows for the generation and computation of microstructures with orientations deviating from the planar isotropic state. The distribution of the predicted damage in the UPPH matrix due to a loading of 2.5% strain in $\boldsymbol{e}_x$-direction is shown in Fig. 14. Basically, we observe a larger distribution of matrix damage for the planar isotropic orientation in comparison to orientations with a preferred alignment in loading direction. The less bundles are oriented in loading direction, the less these bundles can bear the applied loading. Consequently, the loading level in the matrix is higher and so is the general damage level. Occurring damage is distributed in the transition areas between bundles at the bundle tips, and localizes especially at rims of matrix rich areas, see Fig. 14(b) and 14(c). Corresponding analyzes regarding the distributions of bundle damage w. r. t. the orientation are given in Appendix.

6.2. Structural analysis perspective

Utilizing the experimental observations discussed in Section 2.2, we derive different macroscopic failure criteria based on corresponding full-field damage distributions. To investigate the influence of the interaction between fiber bundle orientation and loading direction on the damage evolution and the consequent point of failure, we load generated microstructures with different orientation states (see Fig. 10) in different, non-uniform distributed directions $\boldsymbol{n} \in S^2 = \{\boldsymbol{x} \in \mathbb{R}^3 \mid \|\boldsymbol{x}\| = 1\}$. Therefore, we sample 1000 directions on a unit half sphere with positive $\boldsymbol{e}_z$-direction, see Fig. 15. In analogy to the conducted experiments, we apply an effective uniaxial strain boundary condition in all sampled directions.

For each direction, we compute the damage evolution and the stress response, and evaluate the macroscopic stiffness reduction. For the latter, we compare the current effective stiffness with the initial stiffness in terms of the directional Young's modulus $E(\boldsymbol{n})$ computed via the stress–strain relation $\triangle\, \sigma(\boldsymbol{n}) / \triangle\, \varepsilon(\boldsymbol{n})$. Given a direction $\boldsymbol{n}$, the associated directional stress $\sigma(\boldsymbol{n})$ can be extracted via

$$\sigma(\boldsymbol{n}) = \boldsymbol{\sigma} \cdot (\boldsymbol{n} \otimes \boldsymbol{n}) \,, \tag{6.1}$$

and similarly for the directional strain.

Fig. 16 shows the resulting failure surfaces of a planar isotropic microstructure for different stiffness reductions, derived from the range of reductions known from the experimental observations, see Fig. 5(d). These plots define the maximum allowable stresses for a given level of admissible damage before total failure. Hence, these failure surfaces serve as criterion on a macroscopic integration point level whether a part will sustain a certain stress level or not. For comparability, we depict the failure surfaces in terms of a constrained plot in the $\{\boldsymbol{e}_x, \boldsymbol{e}_y, \boldsymbol{e}_z\}$-space. Note that the negative axes for the stresses in the $\boldsymbol{e}_x$-$\boldsymbol{e}_y$-plane are caused by the corresponding loading directions that point into negative $\boldsymbol{e}_x$- and/or $\boldsymbol{e}_y$-direction, see Fig. 15. The associated directional stress levels themselves are always positive.

Evaluating Fig. 16, the planar isotropic nature of the microstructure is apparent, as the failure surface is rotationally symmetric about the $\boldsymbol{e}_z$-axis, i. e., the directional stress evoking a certain stiffness reduction remains the same irrespective of the loading direction within the $\boldsymbol{e}_x$-$\boldsymbol{e}_y$-plane. Choosing an admissible stiffness reduction of 20% would

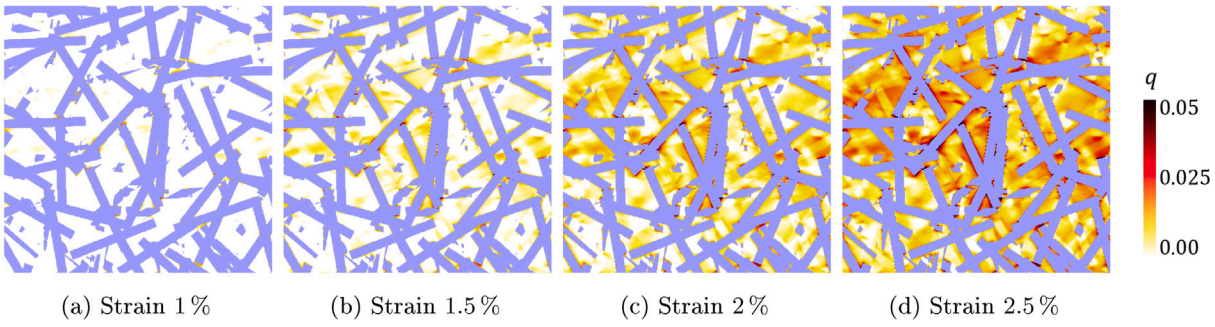

Fig. 13. Evolution of matrix damage during increased loading in vertical direction, in analogy to experimental observations as presented in Fig. 6.

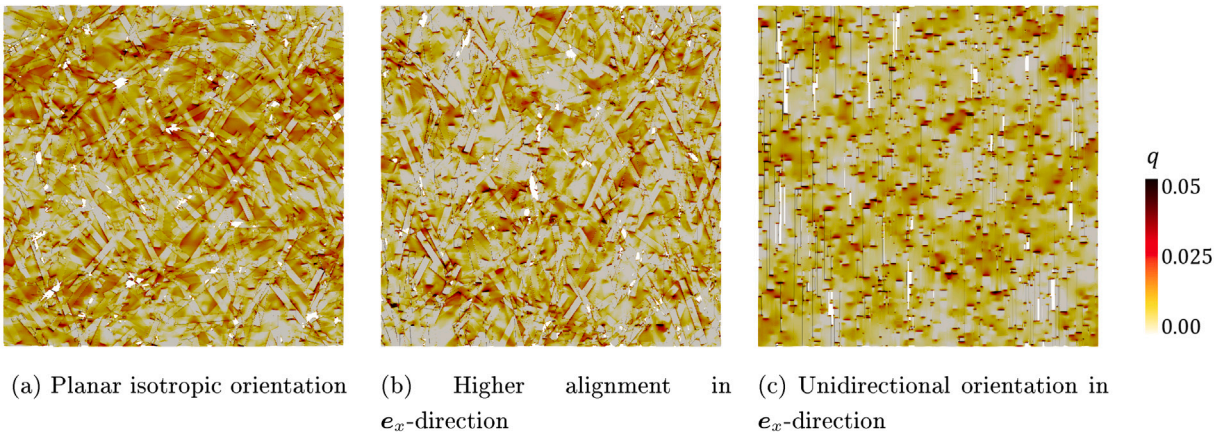

Fig. 14. Predicted UPPH matrix damage according to Section 3.3.1 for different orientations and loading of 2.5% strain in e_x-direction (see Fig. 10 for corresponding microstructures). Bundles are hidden.

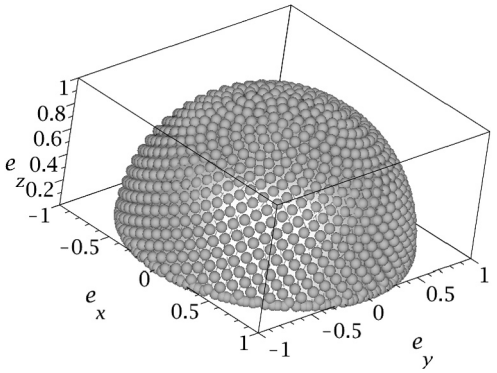

Fig. 15. Sampled directions on unit half sphere.

allow for a directional stress of about 120 MPa in the e_x-e_y-plane, see Fig. 16(b). An increasing e_z-component of the loading direction leads to lower allowed stress levels before failure, as the supporting influence of the fiber bundles decreases for an increasing deviation of the loading direction away from the isotropic e_x-e_y-plane.

Considering a microstructure with bundles being preferably aligned in e_x-direction, see Fig. 10(b), we obtain the failure surfaces shown in Fig. 17. The influence of the non-isotropic bundle orientation is noticeable through the elongated shape of the failure surface in e_x-direction. As more bundles are aligned in e_x-direction, the corresponding stress level is highest and decreases for loadings with increasing components in e_y-direction and/or e_z-direction. For an allowed stiffness reduction of 20%, an SMC composite part with said orientation could bear stresses of up to 250 MPa in e_x-direction and about 75 MPa in e_y-direction, see Fig. 17(b). If we also add a component in e_z-direction with an angle of about 45°, the structure withstands stresses between 75 MPa and 105 MPa before total failure.

For a microstructure with (fully) aligned bundles in e_x-direction, see Fig. 10(c), the resulting failure surfaces follow a similar pattern as for the slight orientation in e_x-direction shown in Fig. 17, but are more pronounced in their extremes, see Fig. 18. Furthermore, the failure surfaces are rotationally symmetric about the e_x-axis, i. e., the admissible stress level remains unchanged for any loading direction in a e_y-e_z-plane. For all loading directions with no component in e_x-direction, the allowed stress level is lowest. The bulges, that become more pronounced for higher stiffness reductions, are caused by the reinforcing character of the fiber bundles for any loading direction with at least a small component in e_x-direction. The bearable stress significantly increases for any loading direction with a non-zero component in e_x-direction, see Fig. 18(d). A further increase of the e_x-component further increases the bearable stress level, but its effect decreases.

6.3. Design perspective

In addition to the structural analysis of our SMC composite, we use our approach to analyze the SMC composite loading conditions from a design perspective. For that case, we consider loadings that evoke specific stress levels, e. g., motivated by given component specifications or boundary conditions, and evaluate the resulting stiffness reduction. The gained knowledge on stiffness reduction due to given stress levels helps identifying and revisiting critical component areas during the design process to counter failure from the start.

To scrutinize the relation between applied stress level and resulting stiffness reduction, we compute the directional-dependent relative residual Young's modulus as

$$\delta(\boldsymbol{n}) = \frac{E(\boldsymbol{n})}{E_0(\boldsymbol{n})} \tag{6.2}$$

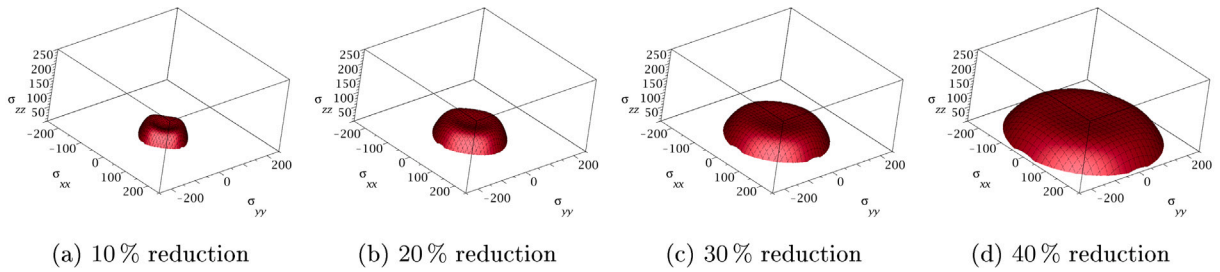

Fig. 16. Failure surface plots for a microstructure with planar isotropic orientation.

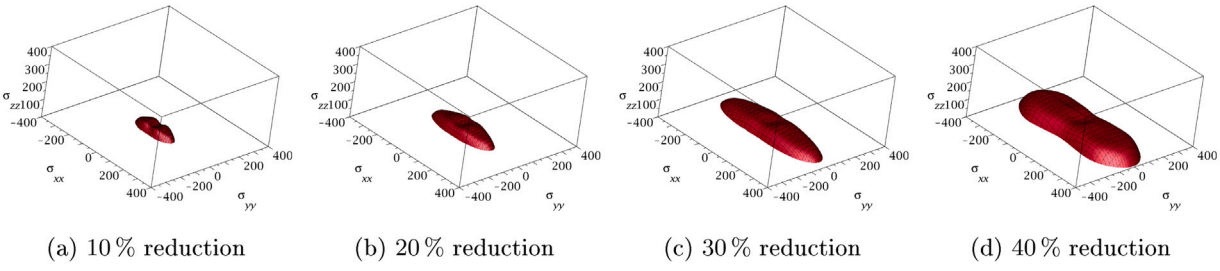

Fig. 17. Failure surface plots for a microstructure with higher alignment in e_x-direction.

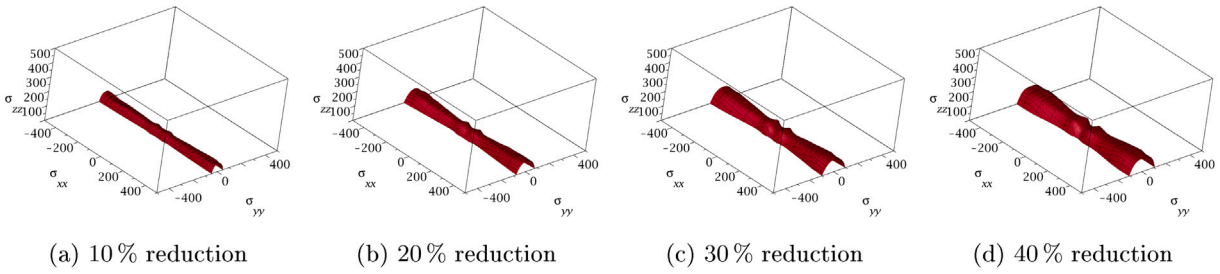

Fig. 18. Failure surface plots for a microstructure with unidirectional orientation in e_x-direction.

via the current (damaged) Young's modulus $E(\boldsymbol{n})$ and the initial Young's modulus $E_0(\boldsymbol{n})$ in a direction $\boldsymbol{n}$. Hence, a value of $\delta(\boldsymbol{n}) = 100\%$ represents a sound Young's modulus in that direction $\boldsymbol{n}$. Similar to the analysis conducted in Section 6.2, we depict the relative residual Young's modulus via iso-surface plots in the $\{e_x, e_y, e_z\}$-space. Note that the negative axes for the relative residual Young's modulus in the e_x-e_y-plane are caused by the corresponding loading directions that point into negative e_x- and/or e_y-direction, see Fig. 15. The associated directional relative residual Young's moduli themselves are always positive.

For a microstructure with planar isotropic orientation, the resulting relative residual Young's modulus plots are shown in Fig. 19. For an applied stress of 10 MPa, the behavior is purely elastic and damage does not initiate yet, which yields a value of $\delta(\boldsymbol{n}) = 100\%$ in all directions, see Fig. 19(a). If the stress level is 60 MPa, damage evolves and the stiffness is reduced, see Fig. 19(b). The stiffness reduction is smallest in the e_x-e_y-plane and highest for loading in out-of-plane e_z-direction, which is in line with the observations made in Fig. 16. The relative residual Young's modulus is rotationally symmetric about the e_z-axis due to the planar isotropic nature of the microstructure. For higher loadings, the relative residual Young's modulus decreases further, as shown in Fig. 19(c). For convenience, we highlighted the undamaged regions with values of $\delta(\boldsymbol{n}) = 100\%$ in the e_x-e_y-plane in gray. A stress level of 180 MPa results in a relative residual Young's modulus within the e_x-e_y-plane of about $\delta(\boldsymbol{n}) = 67\%$, which corresponds to the experimental observations, compare Fig. 19(d) and Fig. 5. If we load the microstructure with a component in e_z-direction having a 45° angle, the relative residual Young's modulus would be $\delta(\boldsymbol{n}) = 53\%$ for the same loading level.

The relative residual Young's modulus plots for an SMC composite microstructure that is preferably oriented in e_x-direction are shown in Fig. 20. For stress levels that induce damage, the relative residual Young's modulus is highest in e_x-direction due to the reinforcing nature of the fiber bundles and decreases towards a loading in e_y-direction. The relative residual Young's modulus is lowest for loadings in out-of-plane e_z-direction, as we lack any supportive effect of the fiber bundles, see Fig. 20(c). For an applied stress of 120 MPa, the relative residual Young's modulus is about 90% in e_x-direction and about 60% in e_y-direction. Similar to observations made in Fig. 19(d), we see the formation of bulges in Fig. 20(d). Even a small proportion of bundles oriented in loading direction have a comparatively high influence on the overall damage evolution, and the relative residual Young's modulus in vicinity of the e_z-direction immediately increases with a comparatively high slope.

The resulting relative residual Young's modulus plots for a microstructure with unidirectionally aligned bundles in e_x-direction are shown in Fig. 21. These plots are rotationally symmetric about the unidirectional e_x-axis. The general behavior is similar to the one observed in Fig. 20, but more extreme. Again, we observe a higher sensitivity of the relative residual Young's modulus in vicinity to loadings in the e_y-e_z-plane and a lower sensitivity for loadings oriented in bundle direction e_x.

7. Summary and conclusions

This work was devoted to identifying macroscopic and anisotropic failure criteria for SMC composites that are motivated by damage evolution on the microscale. Accumulating damage in matrix and bundles in

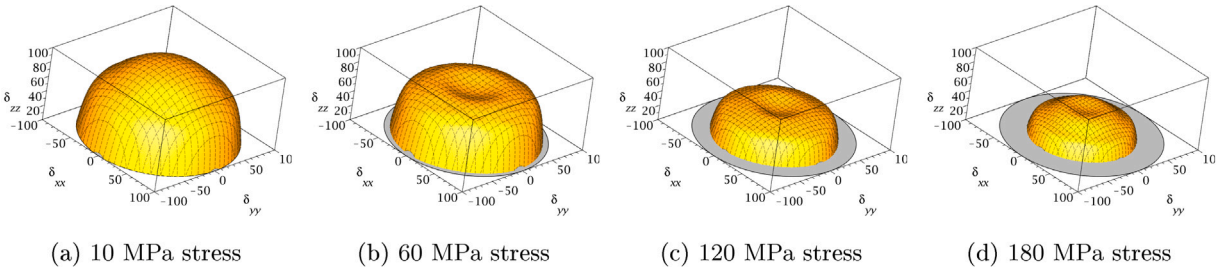

Fig. 19. Relative residual Young's modulus plots for a microstructure with planar isotropic orientation.

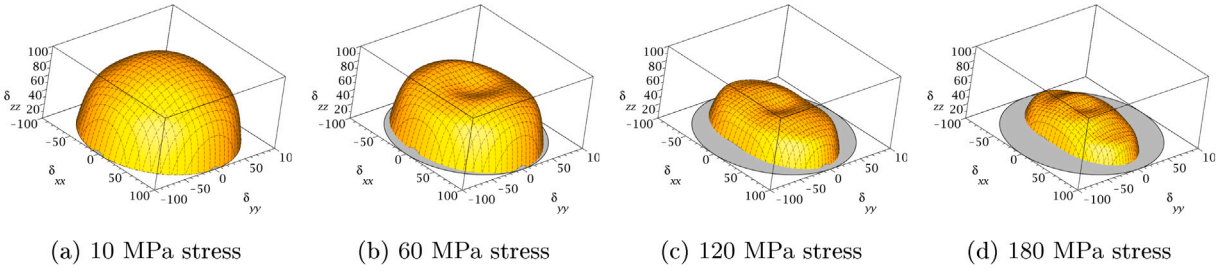

Fig. 20. Relative residual stiffness plots for a microstructure with higher alignment in e_x-direction.

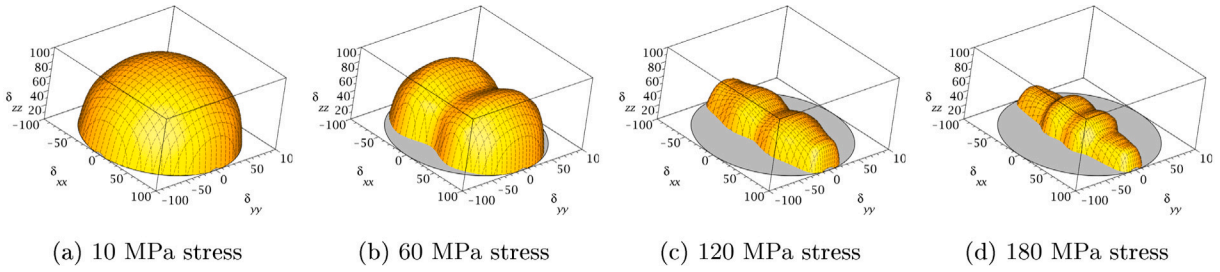

Fig. 21. Relative residual stiffness plots for a microstructure with unidirectional orientation in e_x-direction.

terms of microcracking [20,26,31] on the microscale yields a hardening regime on the macroscale and eventually ends in abrupt failure [12,40].

To capture such a structural behavior, we applied an anisotropic and modular framework [69]. The modular concept allows for the description of fully anisotropic stiffness degradation based on extraction tensors. Inspired by Puck's theory for laminates [73,74], as well as dilatation and distortion, we introduced a number of extraction tensors specifically designed to model damage evolution in SMC composites.

With the help of Bayesian optimization [95], integrating a Mátern 5/2 kernel, an anisotropic distance function for the underlying Gaussian process and an "expected improvement" acquisition function, we were able to identify all necessary parameters in the highly heterogeneous solution space. An implementation combining the experimental results, an FFT-based full-field homogenization approach [56], generated SMC composite microstructures [58] and a corresponding error measure, allowed for a successful minimization of the cost function.

We compared our predicted full-field damage results to corresponding in-situ μCT scan analyzes. Matrix damage in the form of microcracks initiates at the rims of matrix rich regions and is followed by bundle damage. Utilizing generated SMC composite microstructures [58], we transferred our findings onto microstructures with individually selected orientations.

To propel scale-transition, we identified appropriate micromechanics-based anisotropic failure surfaces. We proposed, on the one hand, failure surfaces in stress space considering given admissible stiffness reductions, useful for structural analysis processes. On the other hand, we introduced relative residual stiffness (failure) surfaces based on predetermined component boundary conditions, which are vital for (virtual) design processes. We analyzed the influence of the fiber bundle orientation on both approaches for specific representative microstructures.

The presented framework forms a foundation for a micromechanically and physically motivated database for anisotropic failure criteria on integration point level for SMC composites. In analogy to databases identified for plasticity and short fiber reinforced composites [109,110], a proper discretization and sampling of the orientation space can be established for orientation-dependent SMC composite failure criteria. Furthermore, an uncertainty quantification of the resulting damage and consequent macroscopic failure w. r. t. microscopic parameter variations (such as phase properties or volume fractions) can be investigated. The implemented damage model directly operates on the compliance tensor, which allows for a straightforward coupling of damage evolution to other phenomena such as plasticity [111,112] in future applications.

CRediT authorship contribution statement

Johannes Görthofer: Methodology, Software, Validation, Formal analysis, Investigation, Writing – original draft, Writing – review & editing, Visualization, Project administration. **Matti Schneider:** Conceptualization, Methodology, Software, Resources, Writing – original draft, Writing – review & editing, Supervision, Project administration, Funding acquisition. **Andrew Hrymak:** Conceptualization, Writing – review & editing, Supervision. **Thomas Böhlke:** Conceptualization, Methodology, Resources, Writing – review & editing, Supervision, Project administration, Funding acquisition.

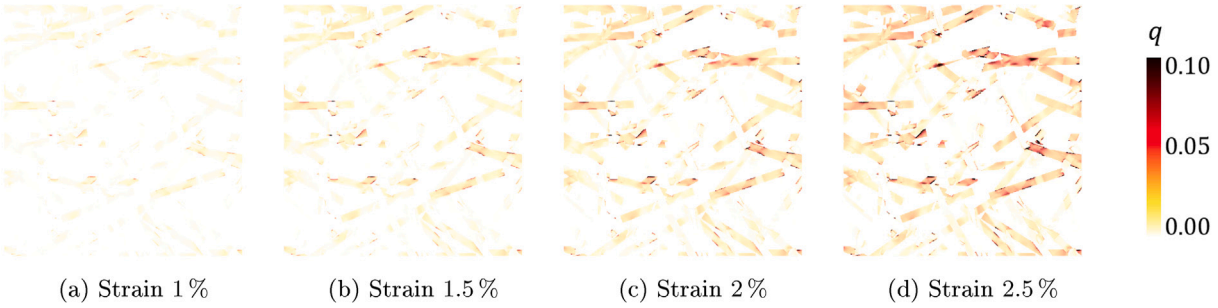

Fig. 22. Evolution of bundle damage perpendicular to bundle direction during increased loading in vertical direction, in analogy to experimental observation as presented in Fig. 6.

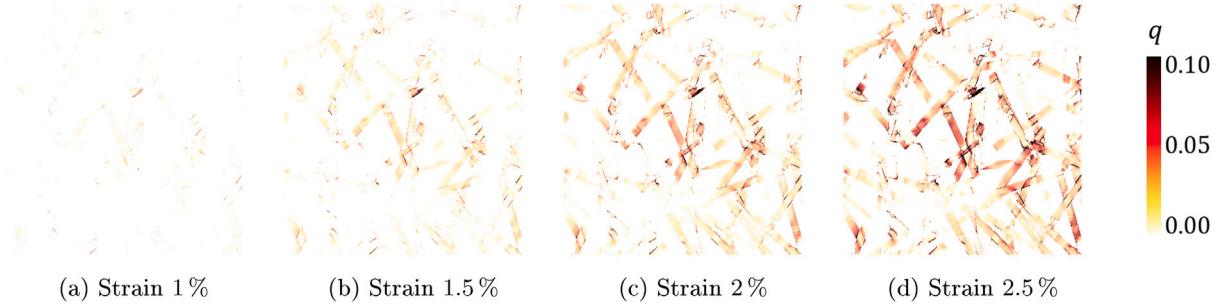

Fig. 23. Evolution of bundle damage in bundle direction during increased loading in vertical direction, in analogy to experimental observation as presented in Fig. 6.

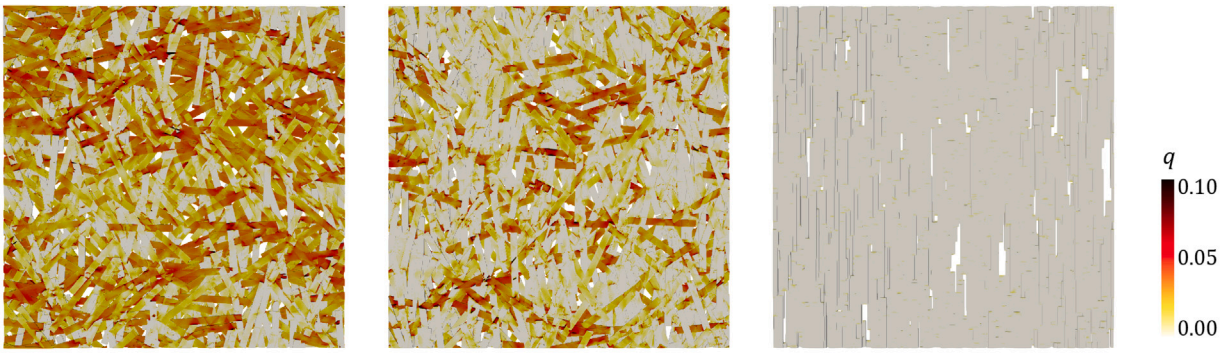

Fig. 24. Predicted bundle damage according to Section 3.4.3 for different orientations and loading in e_x-direction (see Fig. 10 for corresponding microstructures). Matrix is hidden.

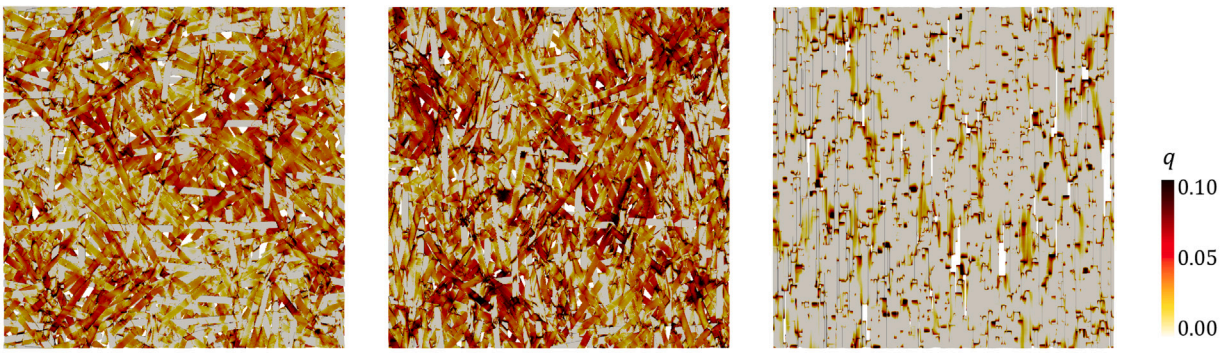

Fig. 25. Predicted bundle damage according to Section 3.4.5 for different orientations and loading in e_x-direction (see Fig. 10 for corresponding microstructures). Matrix is hidden.

Declaration of competing interest

The authors declare that they have no known competing financial interests or personal relationships that could have appeared to influence the work reported in this paper.

Data availability

The raw/processed data required to reproduce these findings cannot be shared at this time as the data also forms part of an ongoing study.

Acknowledgments

JG, MS and TB acknowledge financial support by the German Research Foundation (DFG), Germany within the International Research Training Group 'Integrated engineering of continuous–discontinuous long fiber reinforced polymer structures' (GRK 2078). The support by the German Research Foundation (DFG), Germany is gratefully acknowledged. JG thanks S. Gajek and J. Kuhn for stimulating discussions and M. Bartkowiak, A. Trauth and L. Schöttl for providing experimental knowledge and unhesitating support.

Appendix. Full-field damage evolution for different SMC composite microstructures

An increase of the total loading in combination with evolving matrix damage leads to an increase of load being distributed onto specific fiber bundles. Inevitable, damage is also evoked within these bundles in the form of microcracks running through the bundles along the principal direction and interface debonding. The evolution of bundle damage associated to normal stresses perpendicular to the bundle direction is shown in Fig. 22 for different loading levels in vertical direction (in analogy to Figs. 13 and 6) . The higher the loading, the higher the number of bundles that are damaged and the higher the damage level in certain bundles. Generally, bundles perpendicular to the loading direction encounter the highest damage, whereas bundles in loading direction are hardly damaged for the case at hand, see Fig. 22(d).

Analogously, we encounter damage in bundles due to shear in longitudinal bundle direction, which is shown in Fig. 23. For higher loading levels, bundles that a preferably oriented in loading direction are damaged according to the Puck-type shear criterion, whereas bundles perpendicular to the loading direction are hardly damaged. Hence, our applied Puck-type cases as discussed in Sections 3.4.3 and 3.4.5 are somewhat complementary in their effect on the overall damage evolution, offering a full coverage of possible stiffness degradations in the bundles.

The evolution and distribution of matrix damage is affected by the orientation of the SMC composite microstructure, see Section 6.1. The alignment of bundles is essential, as their reinforcing character is more pronounced the more bundles point into loading direction. Correspondingly, damage in bundles due to normal stresses perpendicular to the principal directions is higher and further distributed, the less fibers are oriented in loading direction, see Fig. 24. In the limit of a pure unidirectional orientation, bundles do not undergo damage perpendicular to their principal direction, see Fig. 24(c).

Damage due to shear stresses in principal bundle direction is also affected by the orientation of the SMC composite microstructure, see Fig. 25. In concurrence with the other damage cases (see Figs. 14 and 24), the damage level of bundles for the considered case is higher, if more bundles are aligned in loading direction, see Fig. 25(b). For an orientation state in vicinity to a unidirectional alignment in loading direction, damage due to shear stresses localizes mainly at bundle tips at the rims of matrix rich areas, see Fig. 25(c). In these regions, bundles are subjected to local stress excesses due to the prior matrix damage, see Fig. 14(c), and hence damage evolution is accelerated.

References

[1] Dumont PJ, Orgéas L, Favier D, Pizette P, Venet C. Compression moulding of SMC: in situ experiments, modelling and simulation. Composites A 2007;38:353–68.
[2] Kim MS, Lee WI, Han WS, Vautrin A. Optimization of location and dimension of SMC pre-charge in compression molding process. Comput Struct 2011;89(15–16):353–68.
[3] Bücheler D. Locally continuous-fiber reinforced sheet molding compound (Doctoral thesis), Karlsruhe Institute of Technology (KIT); 2018.
[4] Wilkinson AN, Ryan AJ. Polymer processing and structure development. Dordrecht: Springer; 1998.
[5] Huang B, Zhao L. Bridging and roughening of short fibers in SMC and parametric optimum. Composites B 2012;43(8):3146–52.
[6] Asadi A, Miller M, Singh AV, Moon RJ, Kalaitzidou K. Lightweight sheet molding compound (SMC) composites containing cellulose nanocrystals. Compos Struct 2017;160:211–9.
[7] Le T-H, Dumont P, Orgéas L, Favier D, Salvo L, Boller E. X-ray phase contrast microtomography for the analysis of the fibrous microstructure of SMC composites. Composites A 2008;39(1):91–103.
[8] Meyer N, Schöttl L, Bretz L, Hrymak A, Kärger L. Direct Bundle Simulation approach for the compression molding process of Sheet Molding Compound. Composites A 2020;132:105809.
[9] Schöttl L, Weidenmann KA, Sabiston T, Inal K, Elsner P. Fiber bundle tracking method to analyze sheet molding compound microstructure based on computed tomography images. NDT & E Int 2021;117:102370.
[10] Brinson HF, Brinson LC. An introduction to polymer engineering science & viscoelasticity. New York, NY: Springer; 2008.
[11] Anagnostou D, Chatzigeorgiou G, Chemisky Y, Meraghni F. Hierarchical micromechanical modeling of the viscoelastic behavior coupled to damage in SMC and SMC-hybrid composites. Composites B 2018;151:8–24.
[12] Trauth A. Characterisation and modelling of continuous-discontinuous sheet moulding compound composites for structural applications (Doctoral thesis), Karlsruhe: Karlsruhe Institute of Technology; 2020.
[13] Bücheler D, Trauth A, Damm A, Böhlke T, Henning F, Kärger L, Seelig T, Weidenmann KA. Processing of continuous-discontinuous-fiber-reinforced thermosets. In: SAMPE Europe conference Stuttgart. 2017, p. 1–8.
[14] Böhlke T, Henning F, Hrymak A, Kärger L, Weidenmann KA, Wood JT, editors. Continuous–Discontinuous fiber-reinforced polymers. Munich: Carl Hanser Verlag GmbH & Co. KG; 2019.
[15] Görthofer J, Meyer N, Pallicity TD, Schöttl L, Trauth A, Schemmann M, Hohberg M, Pinter P, Elsner P, Henning F, Hrymak A, Seelig T, Weidenmann K, Kärger L, Böhlke T. Virtual process chain of sheet molding compound: Development, validation and perspectives. Composites B 2019;169:133–47.
[16] Motaghi A, Hrymak AN. Microstructure characterization in direct sheet molding compound. Polym Compos 2017.
[17] Schöttl L, Dörr D, Pinter P, Weidenmann KA, Elsner P, Kärger L. A novel approach for segmenting and mapping of local fiber orientation of continuous fiber-reinforced composite laminates based on volumetric images. NDT & E Int 2020;110:102194.
[18] Trauth A, Pinter P, Weidenmann K. Investigation of quasi-static and dynamic material properties of a structural sheet molding compound combined with acoustic emission damage analysis. J Compos Sci 2017;1(2):18.
[19] Chen Z, Huang T, Shao Y, Li Y, Xu H, Avery K, Zeng D, Chen W, Su X. Multiscale finite element modeling of sheet molding compound (SMC) composite structure based on stochastic mesostructure reconstruction. Compos Struct 2018;188:25–38.
[20] Fitoussi J, Meraghni F, Jendli Z, Hug G, Baptiste D. Experimental methodology for high strain-rates tensile behaviour analysis of polymer matrix composites. Compos Sci Technol 2005;65(14):2174–88.
[21] Jendli Z, Fitoussi J, Meraghni F, Baptiste D. Anisotropic strain rate effects on the fibre-matrix interface decohesion in sheet moulding compound composites. Compos Sci Technol 2005;65(3–4):387–93.
[22] Kehrer L, Wicht D, Wood JT, Böhlke T. Dynamic mechanical analysis of pure and fiber-reinforced thermoset- and thermoplastic-based polymers and free volume-based viscoelastic modeling. GAMM-Mitt 2018;41(1):1–16.
[23] Arif MF, Meraghni F, Chemisky Y, Despringre N, Robert G. In situ damage mechanisms investigation of PA66/GF30 composite: Effect of relative humidity. Composites B 2014;58:487–95.
[24] Rohrmüller B, Gumbsch P, Hohe J. Microstructural characterization of glass fiber reinforced SMC by nanoindentation and single-fiber push-out test. In: Proceedings of the 4th international conference hybrid 2020 materials and structures, Germany. 2020, p. 1–6.
[25] Schöttl L, Kolb P, Liebig WV, Weidenmann KA, Inal K, Elsner P. Crack characterization of discontinuous fiber-reinforced composites by using micro-computed tomography: Cyclic in-situ testing, crack segmentation and crack volume fraction. Compos Commun 2020;21:100384.

[26] Schöttl L, Liebig WV, Weidenmann KA, Inal K, Elsner P. The use of the empirical crack orientation tensor to characterize the damage anisotropy. Compos Commun 2021;25:100613.

[27] Hohberg M, Kärger L, Bücheler D, Henning F. Rheological in-mold measurements and characterizations of sheet-molding-compound (SMC) formulations with different constitution properties by using a compressible shell model. Int Polym Process 2017;32(5):659–68.

[28] Ben Cheikh Larbi A, Sai K, Sidhom H, Baptiste D. Constitutive model of micromechanical damage to predict reduction in stiffness of a fatigued SMC composite. J Mater Eng Perform 2006;15(5):575–80.

[29] Bartkowiak M, Weit H, Montesano J, Weidenmann KA. Characterization of discontinuous fiber reinforced sheet molding compounds under tension-tension fatigue load. In: Proceedings of the 34th technical conference on composite materials, Vol. 28428. Atlanta, USA: American Society for Composite; 2019, p. 3–10.

[30] Bartkowiak M, Liebig W, Weidenmann KA. Fatigue damage behavior of continuous-discontinuous fiber reinforced sheet molding compounds. In: Proceedings of the 4th international conference hybrid 2020 materials and structures, Germany. 2020, p. 1–7.

[31] Ogihara S, Koyanagi J. Investigation of combined stress state failure criterion for glass fiber/epoxy interface by the cruciform specimen method. Compos Sci Technol 2010;70(1):143–50.

[32] Schemmann M, Lang J, Helfrich A, Seelig T, Böhlke T. Cruciform specimen design for biaxial tensile testing of SMC. J Compos Sci 2018;2(1):12.

[33] Schemmann M, Gajek S, Böhlke T. Biaxial tensile tests and microstructure-based inverse parameter identification of inhomogeneous SMC composites. In: Altenbach H, Jablonski F, Müller WH, Naumenko K, Schneider P, editors. Advances in mechanics of materials and structural analysis: In honor of Reinhold Kienzler, Vol. 80. Springer International Publishing; 2018, p. 329–42.

[34] Schäferling M, Berger D, Häfner B, Lanza G. Data fusion for quality assurance of fibre-reinforced plastics. In: Proceedings of the international symposium on structural health monitoring and nondestructive testing. 2018, p. 1–9.

[35] Bretz L, Wilke M, Häfner B, Lanza G. Comparison of anomaly detection capabilities of pulse phase thermography in transmission and reflection setup on Sheet Molding Compound. In: Proceedings of the 4th international conference hybrid 2020 materials and structures, Germany. 2020, p. 108–15.

[36] Bretz L, Häfner B, Lanza G. Non-destructive measurement of fiber mass content of glass fiber sheet molding compound using Terahertz radiation. Measurement 2021;168:108386.

[37] Fitoussi J, Bourgeois N, Guo G, Baptiste D. Prediction of the anisotropic damaged behavior of composite materials: introduction of multilocal failure criteria in a micro-macro relationship. Comput Mater Sci 1996;5:87–100.

[38] Fitoussi J, Guo G, Baptiste D. A statistical micromechanical model of anisotropic damage for S.M.C. composites. Compos Sci Technol 1998;58(5):759–63.

[39] Fitoussi J, Bocquet M, Meraghni F. Effect of the matrix behavior on the damage of ethylene-propylene glass fiber reinforced composite subjected to high strain rate tension. Composites B 2013;45(1):1181–91.

[40] Meraghni F, Benzeggagh ML. Micromechanical modelling of matrix degradation in randomly oriented discontinuous-fibre composites. Compos Sci Technol 1995;55(2):171–86.

[41] Meraghni F, Blakeman CJ, Benzeggagh ML. Effect of interfacial decohesion on stiffness reduction in a random discontinuous-fibre composite containing matrix microcracks. Compos Sci Technol 1996;56(5):541–55.

[42] Meraghni F, Desrumaux F, Benzeggagh ML. Implementation of a constitutive micromechanical model for damage analysis in glass mat reinforced composite structures. Compos Sci Technol 2002;62(16):2087–97.

[43] Baptiste D. Non linear behavior micromechanical multi-scale modelling of discontinuous reinforced composites. Mater Sci Forum 2003;426–432:3939–44.

[44] Drugan WJ, Willis JR. A micromechanics-based nonlocal constitutive equation and estimates of representative volume element size for elastic composites. J Mech Phys Solids 1996;44(4):497–524.

[45] Guo G, Fitoussi J, Baptiste D. Modelling of damage behavior of a short-fiber reinforced composite structure by the finite element analysis using a micro-macro law. Int J Damage Mech 1997;6:278–99.

[46] Desrumaux F, Meraghni F, Benzeggagh ML. Micromechanical modelling coupled to a reliability approach for damage evolution prediction in composite materials. Appl Compos Mater 2000;7(4):231–50.

[47] Zheng QS, Du DX. An explicit and universally applicable estimate for the effective properties of multiphase composites which accounts for inclusion distribution. J Mech Phys Solids 2001;49:2765–88.

[48] Lee HK, Simunovic S. A damage constitutive model of progressive debonding in aligned discontinuous fiber composites. Int J Solids Struct 2001;38(5):875–95.

[49] Jendli Z, Meraghni F, Fitoussi J, Baptiste D. Multi-scales modelling of dynamic behaviour for discontinuous fibre SMC composites. Compos Sci Technol 2009;69(1):97–103.

[50] Hashin Z, Shtrikman S. A variational approach to the theory of the elastic behaviour of polycrystals. J Mech Phys Solids 1962;10(4):343–52.

[51] Mori T, Tanaka K. Average stress in matrix and average elastic energy of materials with misfitting inclusions. Acta Metall 1973;21(5):571–4.

[52] Willis JR. Variational and related methods for the overall properties of composites. Adv Appl Mech 1981;21:1–78.

[53] Desrumaux F, Meraghni F, Benzeggagh ML. Generalised Mori-Tanaka scheme to model anisotropic damage using numerical eshelby tensor. J Compos Mater 2001;35:603–24.

[54] Duschlbauer D, Pettermann H, Böhm H. Mori–Tanaka based evaluation of inclusion stresses in composites with nonaligned reinforcements. Scr Mater 2003;48(3):223–8.

[55] Schemmann M, Görthofer J, Seelig T, Hrymak A, Böhlke T. Anisotropic meanfield modeling of debonding and matrix damage in SMC composites. Compos Sci Technol 2018;161:143–58.

[56] Schneider M. A review of nonlinear FFT-based computational homogenization methods. Acta Mech 2021;1–50, online.

[57] Matouš K, Geers MGD, Kouznetsova VG, Gillman A. A review of predictive nonlinear theories for multiscale modeling of heterogeneous materials. J Comput Phys 2017;330:192–220.

[58] Görthofer J, Schneider M, Ospald F, Hrymak A, Böhlke T. Computational homogenization of sheet molding compound composites based on high fidelity representative volume elements. Comput Mater Sci 2020;174:109456.

[59] Murakami S, Ohno N. A continuum theory of creep and creep damage. In: Creep in structures. Berlin, Heidelberg: Springer; 1981, p. 422–44.

[60] Chaboche J-L. Continuous damage mechanics - a tool to describe phenomena before crack initiation. Nucl Eng Des 1981;64(2):233–47.

[61] Rahimi AS, Ayatollahi MR, Torabi AR. Elastic–plastic damage prediction in notched epoxy resin specimens under mixed mode I/II loading using two virtual linear elastic failure criteria. Int J Damage Mech 2020;29(7):1100–16.

[62] Sharma A, Daggumati S. Computational micromechanical modeling of transverse tensile damage behavior in unidirectional glass fiber-reinforced plastic composite plies: Ductile versus brittle fracture mechanics approach. Int J Damage Mech 2020;29(6):943–64.

[63] Abu-Farsakh GA, Asfa AM. A unified damage model for fibrous composite laminae subject to in-plane stress-state and having multi material-nonlinearity. Int J Damage Mech 2020;29(9):1329–44.

[64] Wei Q, Gu B, Sun B. Ballistic penetration damages and energy absorptions of stacked cross-plied composite fabrics and laminated panels. Int J Damage Mech 2020;29(9):1465–84.

[65] Onodera S, Okabe T. Analytical model for determining effective stiffness and mechanical behavior of polymer matrix composite laminates using continuum damage mechanics. Int J Damage Mech 2020;29(10):1512–42.

[66] Krajcinovic D. Damage mechanics. Mech Mater 1989;8:3647–79.

[67] Dougill JW. On stable progressively fracturing solids. Z Angew Math Phys 1976;27:423–37.

[68] Ortiz M. A constitutive theory for the inelastic behavior of concrete. Mech Mater 1985;4(1):67–93.

[69] Görthofer J, Schneider M, Hrymak A, Böhlke T. A convex anisotropic damage model based on the compliance tensor. Int J Damage Mech 2022;31(1):43–86.

[70] Halphen N, Nguyen Q. Sur les matériaux standards generalisés. J Méc 1975;14:508–20.

[71] Hansen NR, Schreyer HL. A thermodynamically consistent framework for theories of elastoplasticity coupled with damage. Int J Solids Struct 1994;31(3):359–89.

[72] Wulfinghoff S, Fassin M, Reese S. A damage growth criterion for anisotropic damage models motivated from micromechanics. Int J Solids Struct 2017;121:21–32.

[73] Puck A, Schürmann H. Failure analysis of FRP laminates by means of physically based phenomenological models. Compos Sci Technol 2002;62:1633–62.

[74] Knops M. Analysis of failure in fiber polymer laminates: The theory of Alfred Puck. Berlin, Heidelberg and New York: Springer; 2008.

[75] Revfi S, Mikus M, Behdinan K, Albers A. On the bead design in LFT structures: the influence of manufacturing-induced residual stresses. Des Sci 2021;7.

[76] Orgéas L, Dumont PJ. Sheet molding compounds. Wiley Encycl Compos 2011;1–36.

[77] Trauth A, Kehrer L, Pinter P, Weidenmann K, Böhlke T. On the effective elastic properties based on mean-field homogenization of sheet molding compound composites. Composites C 2021;4.

[78] Pinter P, Dietrich S, Bertram B, Kehrer L, Elsner P, Weidenmann K. Comparison and error estimation of 3D fibre orientation analysis of computed tomography image data for fibre reinforced composites. NDT & E Int 2018;95:26–35.

[79] Li Y, Chen Z, Su L, Chen W, Jin X, Xu H. Stochastic reconstruction and microstructure modeling of SMC chopped fiber composites. Compos Struct 2018;200:153–64.

[80] Moulinec H, Suquet P. A numerical method for computing the overall response of nonlinear composites with complex microstructure. Comput Methods Appl Mech Engrg 1998;157:69–94.

[81] Determination of tensile properties of plastics - Part 4: Test conditions for isotropic and orthotropic fibre-reinforced plastic composites (ISO 527-4: 1997). Berlin, Germany: Deutsches Institut für Normung e.V.; 1997.

[82] Kehrer L, Wood JT, Böhlke T. Mean-field homogenization of thermoelastic material properties of a long fiber-reinforced thermoset and experimental investigation. J Compos Mater 2020;54(25):3777–99.

[83] Trauth A, Pinter P, Weidenmann KA. Acoustic emission analysis during bending tests of continuous and discontinuous fiber reinforced polymers to be used in hybrid sheet molding compounds. Key Eng Mater 2017;742:644–51.
[84] Borwein J, Lewis A. Convex analysis and nonlinear optimization: Theory and examples. New York: Springer; 2006.
[85] Karush W. Minima of functions of several variables with inequalities as side constraints (M. Sc. Dissertation), Dept. of Mathematics, Univ. of Chicago; 1939.
[86] Kuhn HW, Tucker AW. Nonlinear programming. In: Proceedings of the second Berkeley symposium on mathematical statistics and probability. Berkeley: University of California Press; 1951.
[87] Govindjee S, Kay GJ, Simo JC. Anisotropic modelling and numerical simulation of brittle damage in concrete. Internat J Numer Methods Engrg 1995;38:3611–33.
[88] Krawietz A. Passivity, convexity and normality of elastic-plastic materials. Ing-Arch 1981;51:257–74.
[89] Krawietz A. Efficient integration in the plasticity of crystals with pencil glide and deck glide. Tech Mech 2001;21(4):243–50.
[90] Mockus J. Bayesian approach to global optimization. Dordrecht: Kluwer; 1989.
[91] Mockus J. Application of Bayesian approach to numerical methods of global and stochastic optimization. J Global Optim 1994;4(4):347–65.
[92] Noii N, Khodadadian A, Ulloa J, Aldakheel F, Wick T, Francois S, Wriggers P. Bayesian inversion for unified ductile phase-field fracture. 2021, p. 1–61, arXiv:2104.11114.
[93] Bolstad WM, Curran JM. Introduction to Bayesian statistics. John Wiley & Sons; 2016.
[94] Williams CKI, Rasmussen CE. Gaussian processes for machine learning, Vol. 2. The MIT Press; 2006.
[95] Frazier PI. A tutorial on Bayesian optimization, vol. 5, arXiv:1807.02811, 2018, p. 1–22.
[96] Hager W. Updating the inverse of a matrix. SIAM Rev 1989;31(2):221–39.
[97] Matérn B. Spatial variation, Vol. 36. New York: Springer; 2013.
[98] Mockus J, Tiesis V, Zilinskas A. The application of Bayesian methods for seeking the extremum. In: Dixon LCW, Szegö GP, editors. Towards global optimisation 2. North Holland Publishing; 1978, p. 117–29.
[99] Brochu E, Cora VM, De Freitas N. A tutorial on Bayesian optimization of expensive cost functions, with application to active user modeling and hierarchical reinforcement learning. 2010, arXiv:1012.2599.
[100] McKay MD, Beckman RJ, Conover WJ. A comparison of three methods for selecting values of input variables in the analysis of output from a computer code. Technometrics 1979;21(2):239–45.
[101] Behnel S, Bradshaw R, Citro C, Dalcin L, Seljebotn DS, Smith K. Cython: The best of both worlds. Comput Sci Eng 2011;13(2):31–9.
[102] Frigo M, Johnson SG. The design and implementation of FFTW3. Proc IEEE 2005;93(2):216–31.
[103] Schneider M. On the Barzilai-Borwein basic scheme in FFT-based computational homogenization. Internat J Numer Methods Engrg 2018;118(8):482–94.
[104] Gélébart L, Mondon-Cancel R. Non-linear extension of FFT-based methods accelerated by conjugate gradients to evaluate the mechanical behavior of composite materials. Comput Mater Sci 2013;77:430–9.
[105] Wicht D, Schneider M, Böhlke T. On Quasi-Newton methods in fast Fourier transform-based micromechanics. Internat J Numer Methods Engrg 2020;121(8):1665–94.
[106] Paleyes A, Vehtari A, Saul A, Damianou A, Winkelmolen F, Shen H, Hensman J, Gonzalez J, Massiah J, Fass J, Lawrence N, Palm RB, Jenatton R, Kamronn S, Dai Z. GPyOpt: A Bayesian optimization framework in Python. 2016, http://github.com/SheffieldML/GPyOpt.
[107] Thompson WR. On the likelihood that one unknown probability exceeds another in view of the evidence of two samples. Biometrika 1933;25(3/4):285–94.
[108] Advani SG, Tucker CL. The use of tensors to describe and predict fiber orientation in short fiber composites. J Rheol 1987;31(8):751–84.
[109] Köbler J, Schneider M, Ospald F, Andrä H, Müller R. Fiber orientation interpolation for the multiscale analysis of short fiber reinforced composite parts. Comput Mech 2018;61(6):729–50.
[110] Gajek S, Schneider M, Böhlke T. An FE-DMN method for the multiscale analysis of fiber reinforced plastic components. arXiv:2103.08253, vol. 1, 2021, p. 1–33.
[111] Simo J, Ju J. Strain- and stress-based continuum damage models - I. Formulation. Int J Solids Struct 1987;23(7):821–40.
[112] Ju JW. On energy-based coupled elastoplastic damage theories: Constitutive modeling and computational aspects. Int J Solids Struct 1989;25(7):803–33.